

**RETRIEVAL OF THE DIFFUSE
ATTENUATION COEFFICIENT(K_d)
FROM SENTINEL 2 USING THE
2SEACOLOR MODEL AND K_d 'S
IMPACTS ON SENSIBLE HEAT
FLUX OVER NAMTSO LAKE IN
TIBET, CHINA**

PENG ZHANG

February 2018

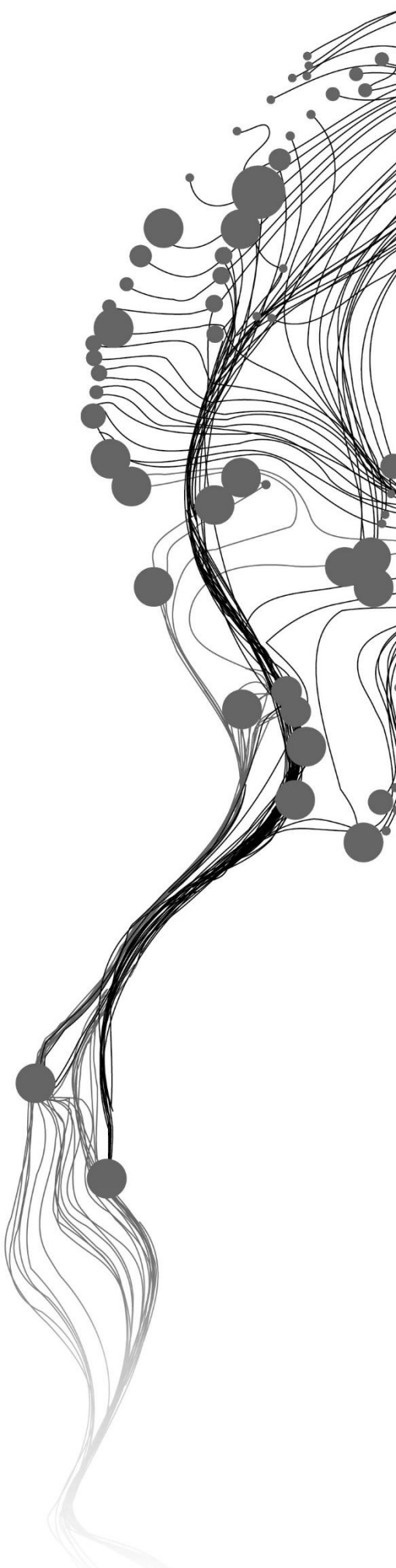
SUPERVISORS:

Dr. Ir. Mhd, Suhyb Salama

Prof. Dr. Z, Su

ADVISOR:

Binbin, Wang



RETRIEVAL OF THE DIFFUSE ATTENUATION COEFFICIENT FROM SENTINEL 2 USING THE 2SEACOLOR MODEL AND K_d 'S IMPACTS ON SENSIBLE HEAT FLUX OVER NAMTSO LAKE IN TIBET, CHINA

PENG ZHANG

Enschede, The Netherlands, February 2018

Thesis submitted to the Faculty of Geo-Information Science and Earth Observation of the University of Twente in partial fulfilment of the requirements for the degree of Master of Science in Geo-Information Science and Earth Observation.
Specialization: Water resources and Environment management

SUPERVISORS:

Dr. Ir. Mhd, Suhyb Salama
Prof. Dr. Z, Su

ADVISOR:

Binbin, Wang

THESIS ASSESSMENT BOARD:

Prof. Dr. Daphne. van der Wal (Chair)
Dr. Jaime Pitarch Portero (External examiner, NIOZ-TEXEL)

DISCLAIMER

This document describes work undertaken as part of a programme of study at Faculty of Geo-Information Science and Earth Observation of the University of Twente. All views and opinions expressed therein remain the sole responsibility of the author, and do not necessarily represent those of the Faculty.

ABSTRACT

Diffuse attenuation coefficient (K_d) for the underwater downwelling irradiance describes the attenuation of incident light in a water column. K_d is a crucial indicator of the aquatic ecosystem quality and heating transfer at the air-water interface. Here, an analytical forward model with an inversion scheme, 2SeaColor model, was employed in combination with Sentinel 2 data to estimate K_d over Namtso Lake in Tibet Plateau, China. Compared to existing models, 2SeaColor model can provide a stable solution for wide ranges of water types in different depth. K_d map was produced by 2SeaColor model over Namtso Lake, and the spatial patterns analysis of K_d map presents that the northeast and northwest of the lake showed higher K_d values and this spatial distribution of K_d could attribute to the determination of the concentration of suspended particulate matters, while the temporal distribution of K_d shared the similar pattern within the eight studied time series from September to December of 2016 and 2017.

In addition, this study also focuses on the correlation between K_d and sensible heat flux. It is known that K_d normally viewed as a constant in the mixed layer model or air-water interaction model. Physically, however, an increase of K_d means more incident solar energy is capping in the water, thus, the K_d impacts on water surface temperature, consequently on sensible heat flux. Therefore, this study firstly performed the correlation analysis between K_d and lake surface temperature which is the MODIS L2 land surface temperature products, and secondly conducted the correlation analysis between K_d and sensible heat flux. The results of correlation analysis showed (1) it is not conclusive that the K_d is correlated to the lake surface temperature in the temporal scale, while (2) most of the pixels in the K_d map and lake surface temperature map present a high correlation coefficient and (3) the correlation coefficient for the K_d and sensible heat flux is -0.85 which indicate that K_d is significantly negatively correlated to sensible heat flux. This study is anticipated that K_d will find function in air-water interaction and mixed layer depth variation.

Keywords: diffuse attenuation coefficient, 2SeaColor model, Namtso Lake, sensible heat flux, correlation analysis

ACKNOWLEDGEMENTS

This work dedicated to my parents (Rongbao Zhang & Ruilan Yang) and my girlfriend.

I would like to extend my gratitude to my supervisor, Dr. Ir. Mhd. Suhyb Salama and Prof. Dr. Z. Su.

I would also like to thank Binbin Wang who collected the field data for me.

TABLE OF CONTENTS

1.	Introduction.....	1
1.1.	Problem definition	2
1.2.	Research objectives	2
1.3.	Research questions	2
2.	Literature review	3
2.1.	K_d with respect to heat transfer at the water-atmosphere interface.....	3
2.2.	Algorithms for estimation K_d	3
2.3.	Light propagation in Namtso Lake	6
2.4.	Sensible heat flux (H).....	6
3.	Study area and datasets	7
3.1.	Study area.....	7
3.2.	Datasets	8
4.	Methodology.....	12
4.1.	Flowchart of methodology	12
4.2.	Models description	13
4.3.	Atmospheric correction (AC) for Sentinel 2 data.....	17
4.4.	Data analysis and accuracy assessment.....	18
4.5.	Verification by Case 2 Regional Coast Colour (C2RCC) algorithm	18
4.6.	The correlation analysis for K_d and H	18
5.	Results.....	21
5.1.	Remote sensing reflectance and K_d from in-situ measurement	21
5.2.	Validation for K_d retrieved by 2SeaColor model.....	22
5.3.	Estimating K_d from Sentinel 2 image	23
5.4.	Verification	26
5.5.	K_d and sensible heat flux (H)	27
6.	Discussion.....	29
6.1.	Assessment of 2SeaColor model	29
6.2.	The spatial and temporal characteristics of K_d in Namtso Lake.....	29
6.3.	The relationship between K_d and H	30
6.4.	The limitations	32
7.	Conclusions.....	32

LIST OF FIGURES

Figure 2-1 Schematic of K_d impacts on H.	3
Figure 2-2 Schematic diagram of retrieving the K_d using the remote sensing method (Su et al., 2011).	4
Figure 2-3 Schematic of the retrieving the K_d form R_{rs}	4
Figure 3-1 Study area: the Namtso Lake. Source: Digital Globe taken on 6 th Mar 2015, ground resolution is 0.46 meters.	8
Figure 4-1 The flowchart of this study.	13
Figure 4-2 The scattering of a water molecule.	14
Figure 4-3 The scattering for a suspended particle.	16
Figure 4-4 Inversion scheme of 2SeaColor model.	17
Figure 4-5 Schematic diagram of temporal correlation.	19
Figure 4-6 Schematic diagram of spatial correlation.	20
Figure 5-1 Field measurements of R_{rs} and K_d spectrum curves (black) with their mean (red) and standard deviation (blue) values.	21
Figure 5-2 Derived K_d (490nm) from 2SeaColor model against known K_d (490nm) from field measurements.	22
Figure 5-3 Derived K_d (490nm) from 2SeaColor model against known K_d (490nm) from convolved field measurements.	23
Figure 5-4 Assessment of AC algorithms with the convolved field measured R_{rs} data in 10m and 60m spatial resolutions.	24
Figure 5-5 K_d (490nm) maps estimated by 2SeaColor model using atmospheric corrected S2 data for Namtso Lake on eight days: (a) 18 th Oct. 2016, (b) 28 th Oct.2016, (c) 6 th Dec.2016, (d) 16 th Dec.2016, (e) 27 th Sept.2017, (f) 17 th Oct.2017, (g) 22 nd Oct.2017, and (h) 1 st Dec.2017.	25
Figure 5-6 The correlation coefficients between K_d and LST.	27
Figure 5-7 The correlation coefficient (r) map for K_d and LST.	28

LIST OF TABLES

Table 2-1 Algorithm for $K_d(490)$ retrieval.....	5
Table 3-1 Ice phenology of Namtso Lake during 2001-2010. Freeze Onset (FO) indicates first ice formation; Freeze-Up (FU) refers to the date that the lake is fully covered by ice; Break-Up (BU) means the date is appearing the detectable ice-free water; Water Clean Ice denotes the end of ablation date that the full disappearance of ice.....	7
Table 3-2 Field measurements.....	9
Table 3-3 The dates of used S2 MSI data.....	9
Table 3-4 S2 MSI Specification.	10
Table 4-1 The coefficients description in the attenuation process.....	14
Table 5-1 The average values (mean) and standard deviations (STD) for the R_{rs} and K_d of selected wavelengths over Namtso Lake.	21
Table 5-2 Statistical parameters of the iCOR and Alcolite AC algorithms in 10m and 60m spatial resolutions.....	24
Table 5-3 The statistic variables of K_d for C2RCC and 2SeaColor models on three days. DR represents dynamic range ($N=10$).....	26
Table 5-4 The meteorological data, computed H and the correlation coefficients.	28

LIST OF ACRONYMS

K_d	Diffuse attenuation coefficient
IOPs	Inherent optical properties
H	Sensible heat flux
G	Heat storage in water
TP	Tibet Plateau
AC	Atmospheric correction
a	Absorption coefficient
b_b	Backscattering coefficient
CZCS	Atmospherically Correct Coastal Zone Colour Scanner
COASTLOOC	Coastal Surveillance through Observation of Ocean Colour
GOCI	Geostationary Ocean Colour Imager
Chl-a	Chlorophyll-a
SPM	Suspended particulate matters
PAR	Photosynthetically Active Radiation
LST	Lake surface temperature
S2 MSI	Sentinel 2 MultiSpectral Instrument
MSTK	MODIS Conversion Toolkit
U	Wind speed
T_a	Near surface temperature
T_s	Lake surface temperature
R_{rs}	Remote sensing reflectance
E_d	Downwelling irradiance
E_u	Upwelling irradiance
L_u	Upwelling radiance
R	Temporal correlation coefficient
r	Spatial correlation coefficient

1. INTRODUCTION

Diffuse attenuation coefficient (K_d in m^{-1}) for underwater downwelling irradiance is a key variable that can quantify the attenuation processes of incident light in a water column. It is a bulk measurement of the light propagation, and it could be used to evaluate heat and evaporation transfer at the water-atmosphere interface on the one hand. On the other hand, K_d can determine whether there is sufficient Photosynthetically Active Radiation (PAR:400-700 nm) that can support photosynthesis in a water column(Stramska & Zuzewicz, 2013; Loiselle et al., 2009; Wu, Tang, Sathyendranath, & Platt, 2007). PAR is fundamental for the aquatic life activities. Thus, K_d is a vital indicator of inland water quality which is of significance to the function of the aquatic ecosystem.

Due to the increasing anthropogenic activities and industry pollutions, a large number of inland waters are deteriorating (Pu, Liu, Qu, & Sun, 2017; Vorosmarty et al., 2010). The traditional methods to quantify and monitor the inland water quality are labour-intensive and time-consuming. Satellite remote sensing compared to the conventional methods can provide an effective way to obtain the water status parameters on spatial-scales (Glasgow, Burkholder, Reed, Lewitus, & Kleinman, 2004; Dekker, Vos, & Peters, 2002). It can also provide synoptic views of the water target over large areas and extend the predictable time periods. Remote sensing can measure the water leaving signals that characterize the optical properties of the water body. The signals recorded by sensors can disintegrate into some sub-signals. These sub-signals stem from the different attenuation processes in the atmosphere, at the water-atmosphere interface, and in the water column. Water leaving reflectance (ρ_w) is the signal of interest as it can be related to IOPs. To obtain ρ_w , atmospheric correction (AC) is needed to remove the interactions between the solar radiation and atmosphere. Therefore, this research performs both atmosphere correction of the signals recorded by sensors and using inversion scheme to quantify the inherent optical properties and then to derive the K_d . From this perspective, with remote sensing technique, the interaction of transmitted solar radiation in a water column with the water constituents can be detected and quantified through IOPs (Mobley, 1994). These IOPs could be absorption and scattering caused by the optically significantly water components and thus determine the K_d . Further, eutrophication and thermal stratification (Liu et al., 2016) often lead to an increase of diffuse attenuation coefficient and water turbidity.

Since the operational algorithm (C2RCC) to retrieve K_d of Sentinel 2 released recently, therefore, in this thesis, the MultiSpectral Instrument (MSI) on-board the Sentinel 2 satellite series designed by European Space Agency (ESA) will be used for retrieved K_d by 2SeaColor model (Salama & Verhoef, 2015) and then validated by corresponding in-situ data as well as verified by C2RCC.

It is studied that K_d affected the incident solar energy partitioning in the water column at different depth by Read, Rose, Winslow, & Read, (2015). Thus, K_d could impact on the water surface temperature, consequently on the heat transfer at the water-atmosphere boundary. Sensible heat flux (H) is one of the important heat flux components in the heat transfer process. Because H is capable of computing by the readily derived temperature. This thesis also analyses the relationship between K_d and sensible heat flux (H) by firstly investigated the dependence of K_d on water surface temperature.

To sum up, the thesis produced the K_d map in varied time series using the 2SeaColor model in combination with Sentinel 2 data attempting to derive the spatial and temporal variations of Namtso Lake in Tibet Plateau (TP). Besides, this thesis also analysed the K_d impact on the water surface temperature and the sensible heat

flux to look for how K_d affect the H. It is expected to provide a robust exploration of the K_d impact on air-water interaction.

1.1. Problem definition

Despite the crucial significance of K_d in the biogeochemical functioning of the inland water system; our current knowledge is incapable of fully understanding the optical complexity of interaction between the light and water components. In addition, most of the previous works developed the algorithms for the remote retrieval of K_d through employing (quasi) single scattering approximation and they normally generate large uncertainty (more than 45%) on derived IOPs to the overall errors over turbid water(Lee, Arnone, Hu, Werdell, & Lubac, 2010a; Salama & Stein, 2009). Some were focused on improving atmospheric correction to obtain a higher accuracy of water leaving reflectance and then deducting the errors of K_d , very little research has been performed to improve the forward model for radiative transfer in water. However, 2SeaColor model developed by is a forward remote sensing model with an inversion scheme for turbid water. 2SeaColor model will be used in this research to investigate the opportunities of Sentinel 2 MSI to estimate K_d in turbid inland water such as Namtso Lake.

Besides, previous studies (Frankignoul, Czaja, & L'Heveder, 1998; Giardino, Pepe, Brivio, Ghezzi, & Zilioli, 2001; Zhang et al., 2015) specified the K_d of the visible part of radiation as a constant value when they are applying the water-heat transfer models and sea surface temperature models and, thus, could result in an inconsistency between model and observation (Denman, 1973). In fact, K_d is with large variations spatially and temporally (Zheng et al., 2016; Tiwari & Shanmugam, 2014). Therefore, it is urged to investigate the spatial and temporal variations of K_d and its relationship between water surface temperature as well as H for the inland waters.

1.2. Research objectives

The main objective of this study is to derive diffuse attenuation coefficient (K_d) for Sentinel 2 data in Namtso lake and to assess the related errors using in situ data.

The specific objectives are:

1. To apply 2SeaColor model to estimate K_d over Namtso Lake.
2. To validate and assess the 2SeaColor model for Sentinel 2.
3. To analyse the spatial and temporal characteristics of K_d in Namtso Lake.
4. To analyse the relationship between K_d and H regarding spatial and temporal variations in Namtso Lake.

1.3. Research questions

The following questions need to be addressed to achieve the objectives mentioned above for this work:

1. Is 2SeaColor model applicable to the Sentinel 2 series satellites?
2. To what extent that the derived K_d map from Sentinel 2 is reliable and applicable?
3. What is the spatial and temporal characteristic of K_d in Namtso lake?
4. What is the relationship between K_d and H with respect to spatial and temporal variations?

2. LITERATURE REVIEW

2.1. K_d with respect to heat transfer at the water-atmosphere interface

The presence of water constituents leads to the increasing of K_d . An increasing K_d value could lead to a reduction of the light penetration along the propagation path within the water column, thus, the temperature of the upper layer of a water body will increase (Chen, Zhang, Xing, Ishizaka, & Yu, 2017). In other words, K_d effects the incident light energy distribution regarding vertical heat transfer within the water. And it is well known that one of the driven mechanism of sensible heat flux (H) is the gradient between surface temperature and air temperature (Brutsaert, 1982), thus K_d plays a role in the heat transfer process at the water-atmosphere interface (Wu, Platt, Tang, & Sathyendranath, 2008). Besides, other physical processes can also influence water surface temperatures, for example, mixing driven by wind or convection (Read et al., 2012), or inflows (Imberger & Patterson, 1980).

Due to the lack of vertical temperature profile data of the Namtso Lake, heat storage in the water body (G) cannot be computed. Thus, this thesis selected the sensible heat flux as the representative of heat transfer progress at the water-atmosphere interface. In summary, Figure 2-1 shows the physical process that K_d impacts on H theoretically.

Some studies were carried out on the importance of K_d with respect to the heat transfer at the water-atmosphere interface. Chang & Dickey (2004) suggested that increased K_d could lead to the greater heat gain at the upper layer of the water body. The gained heat could result in the enhancement of the thermocline and lagging of the Chl-a in the eutrophic depth. Wu et al. (2007) studied the bio-optical heating caused by K_d increasing and its contribution to upper dynamics in the Labrador Sea. The impact of K_d on sea surface temperature was investigated by Wu et al. (2007) through comparing the mixed layer model that employed the modelled K_d and an assumed constant K_d . Their results showed the sea surface temperature increased 1 °C at most of the sea and up to 2.7 °C at the high K_d value area.

However, there are other factors also determine the H , for instance, air temperature, wind speed, atmospheric stability (Wang, Ma, Ma, & Su, 2017) except for K_d . Hence, it is complicated to find the relation between K_d and H .

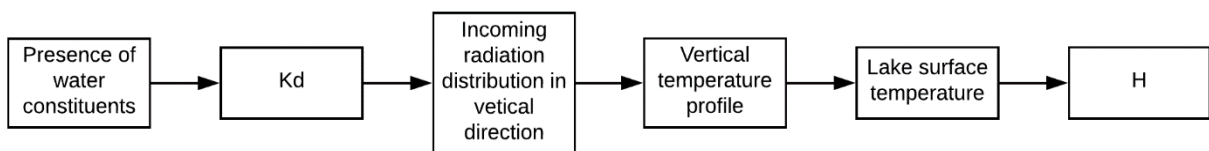


Figure 2-1 Schematic of K_d impacts on H .

2.2. Algorithms for estimation K_d

Figure 2-2 explicated the sources of signals using the remote sensing method to retrieve the K_d for the inland water system, i.e. water constituents, adjacent land pixels, and atmosphere. Obviously, in order to derive K_d , atmospheric correction (AC) algorithm and K_d retrieval algorithm are indispensable. A reliable AC algorithm was implemented to remove the atmospheric interaction and the adjacent effect. AC algorithm is going to be elaborated in the following part. Apart from AC, the analytical K_d retrieval algorithms focus on the signal inside of the water.

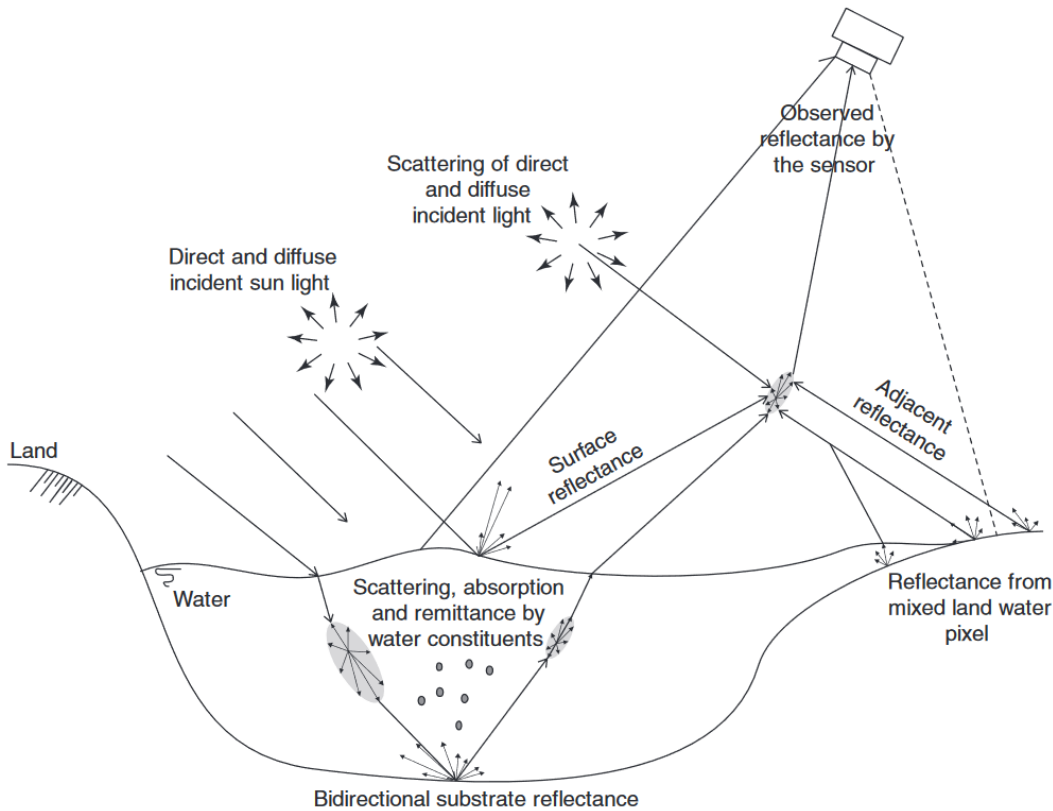


Figure 2-2 Schematic diagram of retrieving the K_d using the remote sensing method (Su et al., 2011).

The models used for estimating K_d can be categorised into two types. The first ((a) in Figure 2-3) is the empirical model which based on the band ratio. The second ((b) in Figure 2-3) is based on the derived IOPs (i.e. absorption coefficient (a) and the backscattering coefficient (b_b)). The relationship between K_d and IOP could be “semi” analytical or empirical both. And the details are unfolded below.

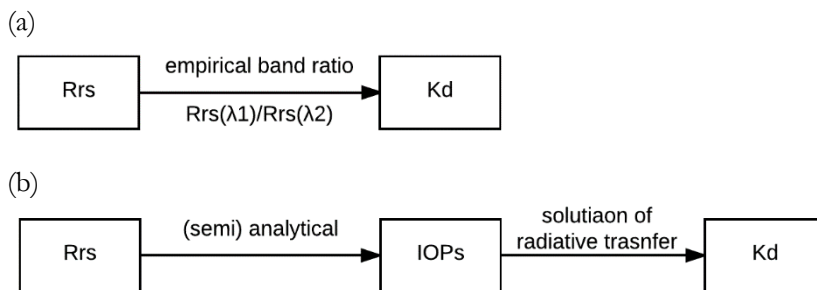


Figure 2-3 Schematic of the retrieving the K_d form R_{rs} .

(a) Empirical models based on band ratio

Austin & Petzold (1981) developed an empirical algorithm to derive K_d (490) from Atmospherically Correct Coastal Zone Colour Scanner (CZCS) data utilising the blue-green ratio of upwelling radiances above water (L_w). All the algorithms discussed in this part showed in Table 2-1. A slightly modified approach was proposed by Kratzer, Brockmann, & Moore (2008) to retrieve K_d (490) from Medium Imaging Spectrometer

(MERIS) data. Besides, two-step empirical algorithm with a concentration of chlorophyll as an intermediate link also developed (O'Reilly et al., 1998). This model developed by O'Reilly et al. (1998) is to first derive the concentration of chlorophyll, Chl, from remote sensing reflectance and then related it to K_d using empirically derived relationships. The spectrum ratio-based models are normally working well in clear water where the optical properties mainly governed by the presence of phytoplankton and its decomposed product. But they generally produce huge errors in turbid waters due to the complexed water components and intrinsic limitation of empirical models based on band ratio (Lee et al., 2005; Lee et al., 2010; Salama, Mélin, & Van der Velde, 2011).

Zhang & Fell (2007) developed a piecewise function which contains two independent algorithms under different conditions to derived K_d . This improved empirical model developed by Zhang & Fell (2007) used NOMAD in-situ data to define the model coefficients and used the Coastal Surveillance through Observation of Ocean Colour (COASTLOOC) in-situ data to validate. This model extends the range of applicability which means it also performed well in the turbid water.

Table 2-1 Algorithm for K_d (490) retrieval.

Type	Algorithm	Reference
	$K_d(490) = 0.022 + 0.088 \left(\frac{L_w(443)}{L_w(550)} \right)^{-1.491}$	Austin & Petzold (1981)
Empirical band ratio	<p>If $\frac{R_{rs}(490)}{R_{rs}(555)} \geq 0.85$ then $K_d(490) = 10^{(-0.843 - 1.459X - 0.101X^2 - 0.811X^3)} + 0.016$</p> <p>Where $X = \log_{10} \left(\frac{R_{rs}(490)}{R_{rs}(555)} \right)$;</p> <p>If $\frac{R_{rs}(490)}{R_{rs}(555)} \leq 0.85$ then $K_d(490) = 10^{(-0.094 - 1.302X + 0.247X^2 - 0.021X^3)} + 0.016$</p> <p>Where $X = \log_{10} \left(\frac{R_{rs}(490)}{R_{rs}(665)} \right)$;</p>	Zhang & Fell (2007)
Empirical IOP	$K_d(490) = (1 + 0.005\theta_s)a(490) + 4.18(1 - 0.52e^{-10.8a(490)})b_b(490)$ $K_d(490) = (1 + \cos \theta_s)a(490) + (a(490)^4 + a(490))^{0.01}$	Lee et al. (2005) Simon & Shanmugam, (2016)
Fully analytical	$K_d = \frac{((k-s')E_{ds} + \alpha \cdot E_{dd} - \sigma \cdot E_u)}{E_d}$ (details in the method part)	Salama & Verhoef (2015)

(b) Models based on IOPs

The model proposed by Lee (Lee, Du, & Arnone, 2005; Lee et al., 2005; Lee et al., 2002) is based on deriving IOPs using the QAA (quasi-analytical algorithm) and then relating K_d to derived IOPs (i.e. absorption coefficient (a) and backscattering coefficient (b_b)) and boundary conditions such as solar zenith angle. Therefore, this algorithm proposed by Lee (Lee, Du, & Arnone, 2005; Lee et al., 2005; Lee et al., 2002) retrieves the K_d through two steps. The first step is to obtain IOPs from remote sensing reflectance using spectrum optimisation. And the second step is to derive K_d from obtained values of IOPs. Another semi-analytical model is developed by Simon & Shanmugam (2016) for retrieving K_d . The model developed by Simon & Shanmugam (2016) only considered the absorption coefficient at 490 nm as the key variable.

Further, their results of the model validated by a large number of field measurements and also compared to others existing models.

Compared to these models, Salama & Verhoef (2015) developed a fully analytical model, 2SeaColor model, with an inversion scheme to derive the diffuse attenuation coefficients from the remote sensing satellite data. This 2SeaColor model projects the effect of turbidity on the inherent optical properties which is one of the differences between the quasi-single scattering models. Thus, the 2SeaColor model is appropriate for retrieving the K_d both for clear and turbid water. In addition, 2SeaColor model can derive the depth profile of K_d in a homogenous water layer. Besides, being an analytical model, the 2SeaColor model does not contain the empirical coefficients. As a result, the application of 2SeaColor model without limitation of a particular region. Yu, Salama, Shen, & Verhoef (2016) proposed an improvement on the parameterisations in the inverse scheme of the 2SeaColor model. The results of Yu et al. (2016) showed the reasonable magnitude and range of K_d over Yangtze Estuary had been produced when applying the improved 2seacolor model on the Geostationary Ocean Colour Imager (GOCI) data.

2.3. Light propagation in Namtso Lake

K_d describes the propagation of incoming light in a water column. Normally, the researchers pay more attention to the K_d at a certain wavelength, for example, 490nm. While, due to a rare study carried on K_d at a specific wavelength at Namtso Lake, this part introduced K_d (PAR) for Namtso Lake. K_d (PAR) calculate by a weighted average of K_d values at a wavelength between 400 to 700 nm. In fact, the K_d (PAR) also reflected the light propagation situation but only within the wavelength of 400 to 700nm.

Wang et al. (2009) measured the PAR at Namtso Lake. The result shows that (1) the average value of PAR is $2622 \mu\text{mol}^{-1}\text{m}^{-2}$ which indicated strong solar radiation in the Namtso area, (2) there are two types of the vertical changing trend of PAR. One is exponentially declined from $4650 \mu\text{mol}^{-1}\text{m}^{-2}$ at the surface to $100 \mu\text{mol}^{-1}\text{m}^{-2}$ at a depth of 30 m. The other is a single sub-peak value appeared at the depth of 4-7 m, (3) the diffuse attenuation coefficient of PAR, K_d (PAR), ranges from 0.07 to 0.17 m^{-1} with an average of 0.12 m^{-1} and there are no obvious spatial variations.

Nima et al. (2016) suggested the K_d (PAR) in the range of 0.12-0.16 m^{-1} which is similar to the previous study. The result of Nima et al. (2016) also indicated that absorption by phytoplankton at 440 and 676 nm, dedicatedly due to the very low concentration of chlorophyll-a (Chl-a) in Namtso Lake. In addition, CDOM is seen to be the dominant absorbing component at the UV wavelength of 380 nm and the visible wavelength of 443 nm in this lake.

2.4. Sensible heat flux (H)

Sensible heat flux is a pivotal variable in the heat and water budget. Haginoya et al. (2009) calculated the sensible heat flux using the heat balance equation over Namtso Lake throughout one year. The Lake Surface Temperature (LST) and other meteorological data stem from the combination of Earth observation data and Ground Weather Station data. According to the results of seasonal variation analysis, the sensible heat flux was very small from February to July (pre-monsoon and mid-monsoon) whereas H is increasing dramatically from October to January. It showed a typical deep lake feature that can provide a tremendous heat to the atmosphere during post-monsoon. Wang et al. (2015) simulated the water-atmosphere heat transfer process by using a bulk aerodynamic transfer model over so-called small Namtso Lake. Based on Eddy Covariance (EC) measurements, Wang et al. (2015) indicated that with the presence of large water-atmosphere gradients and strong wind, the wind speed dominates the heat transfer of the interface between water and atmosphere. The other research (Wang, Ma, Ma, & Su, 2017) focused on physical control on different temporal scales of turbulent heat flux exchange over the small Namtso Lake. They indicated that the wind speed dominated the half hourly scale while water vapour and temperature difference tie the daily

and monthly scale of turbulence fluxes closely. However, this thesis investigated the relationship between K_d and sensible heat flux at the same moment instead of within a time period. It means the instantaneous H is more susceptible to the environment variables such as wind speed and air temperature. Therefore, it is a challenge to look for the relationship between K_d and H .

3. STUDY AREA AND DATASETS

3.1. Study area

Namtso Lake (black area in Figure 3-1) is a mountain lake located in the Tibet Autonomous Region of China, approximately 112 kilometres north-northwest of Lhasa. The lake lies at an elevation of 4718 m above sea level and has a surface area of 1920 km² with the average depth of 33m and the maximum depth of 98.9 m(Wang et al., 2009). The length and width of the lake are approximately 65km and 40km, respectively. In addition, the ice phenology was investigated by Kropáček, Maussion, Chen, Hoerz, & Hochschild, (2013) and Ke, Tao, & Jin, (2013) showed below because the lake ice blocks the water-atmosphere, consequently obstructed the heat transfer between the lake and atmosphere, while, sublimation does not compensate this effect. Therefore, the analysis of ice phenology of Namtso Lake showed in Table 3-1 according to the previous study (Kropáček et al., 2013). But as the temperature of Namtso Basin trends to increase rapidly, the ice-free duration has been extended (Ke et al., 2013). Besides, the Namtso Lake is a subsaline lake (degree of mineralisation is 1.78 g·l⁻¹ based on the survey data in 1979), but researcher argued that it is gradually becoming salty (Guan et al., 1984).

Table 3-1 Ice phenology of Namtso Lake during 2001-2010. Freeze Onset (FO) indicates first ice formation; Freeze-Up (FU) refers to the date that the lake is fully covered by ice; Break-Up (BU) means the date is appearing the detectable ice-free water; Water Clean Ice denotes the end of ablation date that the full disappearance of ice.

Name	Mean FO	Mean FU	Mean BU	Mean WCI
Namtso Lake	4 Jan	14 Feb	4 Apr	15 May

Namtso Lake is a closed lake which is supplied mainly by precipitation and glacier meltwater which formed more than 60 rivers from the Nyainqentanglha Range (Guan et al., 1984; Wang et al., 2010). Grey silt, fine sand, and fine clay sand regulate the suspended particulate matter in the Namtso lake which contains considerable carbonate. Barrier beaches formed of gravel, with some of them already cemented by calcic materials, are a major source of lakeshore deposits (Zhu et al., 2004). The dominant cations and anion are the Ca⁺ as well as Na⁺ and HCO₃⁻ in the lake and its inflowing river water (Wang et al., 2010).

During the August-September season, the vertical profile of this lake can be classified according to the thermal stratification of three layers which are the epilimnion, metalimnion, and hypolimnion. The vertical fluctuation of diffuse attenuation coefficient is influenced by the existence of these distinguished layers while the spatial variations are not obvious (Liu & Chen, 2000; Wang et al., 2009).

Climatically, the study area is located in the transition zone that mainly impacted by the westerlies in winter and Indian summer monsoons in summer. Strong wind often occurs in winter, and the dominate wind direction is west-east controlled by westerlies. While, in summer, wind with low velocity forms (Kropáček et al., 2013).

Due to the unique characteristics, Namtso Lake as the largest lake in the centre of Tibet and since its remote and inaccessibility, it is considered to the sensitive indicator of environmental and regional even global climate changes (Liu et al., 2016).

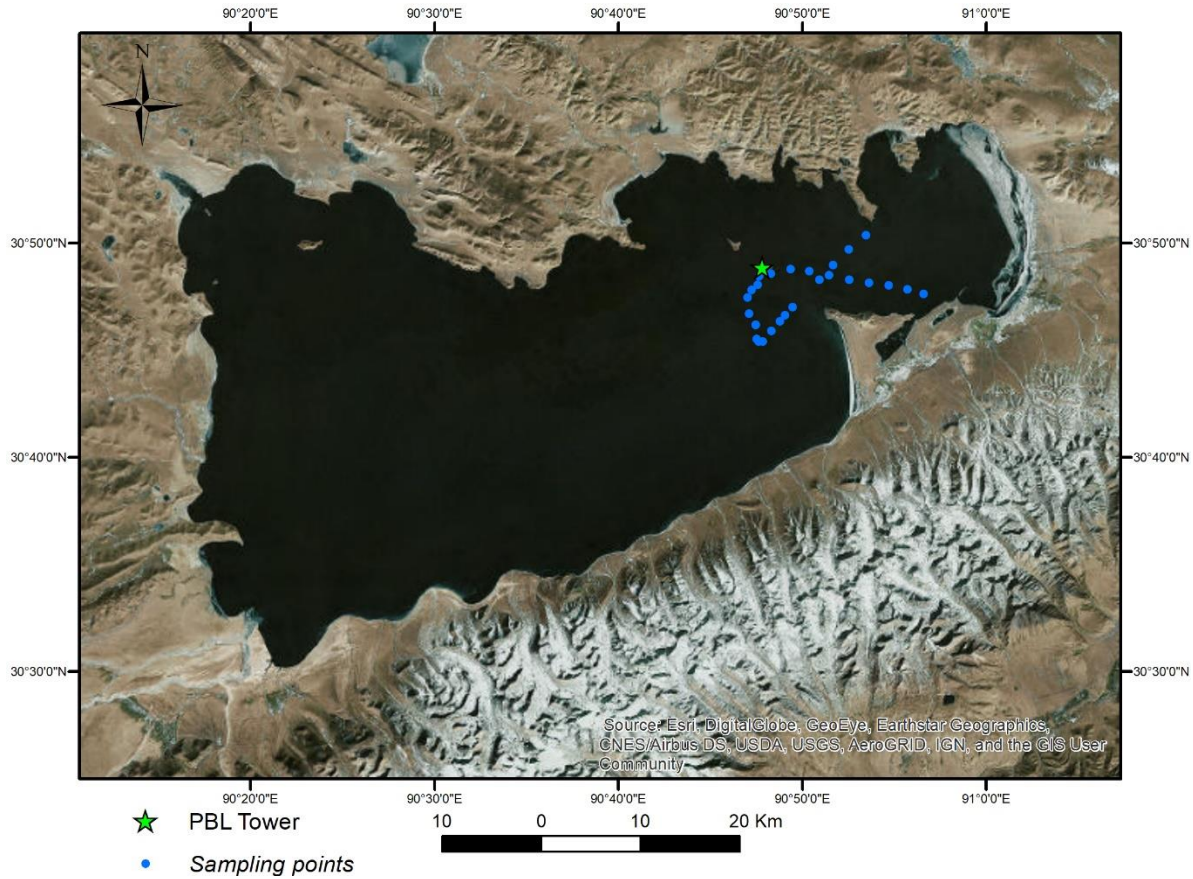


Figure 3-1 Study area: the Namtso Lake. Source: Digital Globe taken on 6th Mar 2015, ground resolution is 0.46 meters.

3.2. Datasets

3.2.1. In-situ data over Namtso Lake

In-situ data (blue dots in Figure 3-1) over Namtso lake consist of above-water upwelling radiance (L_u in SI unit of $W \cdot m^{-2} \cdot sr^{-1}$) as well as above-water downwelling irradiance (E_d in SI unit of $W \cdot m^{-2}$) and the underwater downwelling planar irradiances at two depths, 0.3 m and 0.6 m ($E_d(z_1)$ and $E_d(z_2)$) of Namtso Lake. In addition, the spectral resolution and the sampling interval are 3.3 nm and 1 nm, respectively. Also, the in-situ data including the corresponding location which is latitude and longitude recorded by GPS. The solar zenith angle was between 40° to 15° for all field data. Remote sensing reflectance (R_{rs}) was calculated by the L_u and E_d as $R_{rs} = L_u / E_d$. E_d retrieved the K_d in two depths as:

$$K_d = \frac{1}{\Delta z} \ln \frac{E_d(z_1)}{E_d(z_2)}$$

This radiometric information collected by TriOS Ramses sensors, more detail can be derived from <http://www.trios.de/>

The data collection performed on 26th, 27th and 28th of May 2017, 60 datasets in total. The data quality checking (QC) analysis was performed with three steps: First, retrieving K_d by 2SeaColor model and

validating by the field K_d data. Second, inspecting if the shapes of the outliers are abnormal or turbulent. Third, deleting the turbulent data. According to the result of the quality check, 17 datasets were selected for the further analysis.

The L_u and E_d values recorded by TriOS Ramses sensors equal to the diffuse and direct of the natural solar radiation. Thus, the L_u and E_d values depended strongly on the weather condition when the measurement executed. Table 3-2 shows the information of field data collection. The maximum values of L_u and E_d could reach $21.55 \text{ mW}\cdot\text{m}^{-2}\text{nm}^{-1} \text{ sr}^{-1}$ and $1249.77 \text{ mW}\cdot\text{m}^{-2}\text{nm}^{-1}$ and the minimum could reach $0.51 \text{ mW}\cdot\text{m}^{-2}\text{nm}^{-1} \text{ sr}^{-1}$ and $57.27 \text{ mW}\cdot\text{m}^{-2}\text{nm}^{-1}$ during sunny midday among all the measurements. These radiance and irradiance values indicated that the solar radiation intensity over the Namtso lake in the summer season is strong. In general, the $E_d(\lambda)$ spectra has a high magnitude in the blue-green region. The spectra of $K_d(\lambda)$ (Figure 5-1) is flat at the wavelength smaller than 700 nm and increase at the NIR band because the water molecules have a strong absorption effect at NIR. During the in-situ data collection, the solar zenith angle of Namtso Lake ranges from $49.25^\circ\sim 12.55^\circ$.

Table 3-2 Field measurements.

Sampling date	Sampling time (GMT+8)	Number of points	Number of points (after QC)	Weather condition
26 th May 2017	10:07-14:57	14	4	Cloudy
27 th May 2017	11:18-14:55	36	13	Cloudy
28 th May 2017	10:51-12:55	10	0	Cloudy
Total	/	60	17	/

3.2.2. Sentinel 2 MSI (S2 MSI) data and atmospheric correction

S2 MSI data has proven to be suitable for calculation of the water reflectance and thus retrieval of the water quality variables (Vanhellemont & Ruddick, 2016). Therefore, the Sentinel 2 was selected as the input of 2SeaColor model to estimate K_d over Namtso Lake.

The corresponding S2 MSI data for validation should also be collected in 26th and 27th of May of 2017 with minimal cloud cover. Unfortunately, only the data of 15th of May is available for the validation due to the others are contaminated by cloud. Besides, because the TP features favourably low cloud cover during winter, eight scenes of S2 MSI data from September to December of 2016 and 2017 were collected for investigating the correlation between K_d and H. The dates of used S2 MSI data were shown in Table 3-3. Also, the acquisition time of S2 MSI over Namtso Lake is around 04:41 to 04:45(UTC). The solar zenith angle for all S2 data is ranging from 34° to 57° . In addition, a simple linear relationship was established to shift wavelengths at 440 nm, 660 nm, 700 nm, and 780 nm of the field data to the corresponding wavelengths at 443 nm, 665 nm, 705 nm, and 783 nm of S2 data due to the different channel setting between S2 and field radiometric measurements. The determination coefficients larger than 0.99 were selected for the further analysis.

Table 3-3 The dates of used S2 MSI data.

Year	2016	2016	2016	2016	2017	2017	2017	2017
Month	10	10	12	12	9	10	10	12
day	18	28	6	16	27	17	22	1

The spatial resolution of S2 is dependent on the particular spectral band. The 10 m spatial resolution bands are B2 (490 nm), B3 (560 nm), B4 (665 nm) and B8 (842 nm); The 20 m resolution bands are B5 (705 nm), B6 (740 nm), B7 (783 nm), B8a (865 nm), B11 (1610 nm) and B12 (2190 nm); The 60 m resolution bands are B1 (443 nm), B9 (940 nm) and B10 (1375 nm). Table 3-4 shows the detail of Sentinel 2 specification. In addition, the level 1C product of Sentinel 2 MSI which gives the Top of Atmosphere (TOA) reflectance has already performed the radiometric and geometric correction, and hence it was used in this research to derive K_d . Besides, the lake was clipped into two tiles of S2 data when downloading from the S2 data hub and thus mosaicking was performed. The pixel values of mosaic images are using the arithmetic mean of pixels for the two tiles.

Table 3-4 S2 MSI Specification.

Spatial resolution (meters)	Revisit time (days)	SWATH width (km)	Spectral bands	Spectral range (nm)
10,20,60	5	290	13	443-2190

For the aquatic application earth observation, the atmospheric correction (AC) is indispensable. The AC of S2 MSI data implemented by iCOR and Alcolite algorithm. Both these two AC algorithms are state-of-the-art and designed for aquatic application among S2 dedicatedly. iCOR is a plugin embedded in the Sentinel Application Platform (SNAP). SNAP is a software designedly developed by Telespazio Germany (TPZV) on behalf of ESA for the processing and analyzing the Sentinel 2 series data. The other alternative AC algorithm is Alcolite which can run in the Python environment. After performing the AC, the level 2A product was derived. The level 2A product includes the main output of Bottom of Atmosphere (BOA) corrected reflectance product and the additional product of an Aerosol Optical Thickness (AOT) map, a Water Vapor (WV) map etc.

The details of these two AC algorithms could be found in the part of Methodology.

3.2.3. Meteorological and Land Surface Temperature (LST) data

One of the objectives of this study is looking for the relation between K_d and H. However; it is hard to observe the relation between K_d and H directly due to the dynamic nature of the water surface and atmosphere. Hence, in order to analyse the relation between K_d and H, the study of the relation between K_d and Lake Surface Temperature (LST) was first performed.

To begin with, there are several substitutes for the LST data such as (1) interpolating the surface temperature form the automatic weather stations (AWS) which can provide the Namtso Lake surface temperature, (2) using mathematical models to calculate the LST data from S2 MSI, (3) using the MODIS LST data directly. However, with considering the temporal and spatial resolution as well as the amount of data processing, the MODIS LST data was selected to perform the analysis.

The MODIS instrument onboard the Terra and Aqua spacecrafts. They provide global coverage every day in 36 discrete spectral bands with viewing swath width of 2330 km. Terra's/Aqua's sun-synchronous, the near-polar circular orbit is timed to cross the equator from north to south/south to north (descending/ascending node) at approximately 10:30 a.m./p.m. local time. Additionally, some previous studies (Xiao et al., 2013; Crosman & Horel, 2009) showed that MODIS/Terra LST product could provide a better performance in terms of determination coefficient, bias, and RMSE than the MODIS/Aqua product. Also given the amount of data processing, the level 2 LST MODIS/Terra version 6 product (MOD11_L2), therefore, with the corresponding acquisition dates of Sentinel 2 were collected and processed for this study. It has to be mentioned that the level 2 MODIS products were swath data without geolocation system. Hence, the level 2 product was georeferenced and projected by ENVI plugin, MODIS Conversion Toolkit (MCTK) 2.1.7, developed by Devin White. The MCTK released on GitHub

<https://github.com/dawhite/MCTK>. The LST MODIS/Terra product was reprojected onto WGS84/UTM Zone 46N which was corresponding to S2 data. More information could be found in the User's Guide of MCTK.

The overpass time of MODIS recorded in coordinated universal time (UTC). MODIS/Terra LST products provided two times (daytime and night time) per day measurements (Hu, Brunsell, Monaghan, Barlage, & Wilhelmi, 2014). The MODIS/Terra overpass time for Namtso Lake is about 04:05 to 05:25 (UTC) (daytime) and 15:40 to 16:45 (UTC) (night-time) in the study period, respectively. Concerning the acquisition time of S2 MSI, the daytime MODIS/Terra product was selected for the further analysis. However, the daytime MODIS/Terra product on the days of 18th October.2016, 28th October.2016, 16th October.2016, and 1st December.2017 were not available because of the cloud contamination, thus, the night-time MODIS/Terra products instead as the proxies.

The spatial resolution of MOD11_L2 product is 1 km. Due to the size of the Namtso Lake (L: 65 km, W: 40 km), the resolution of the MOD11_L2 product is acceptable. The MOD11_L2 product is the result of the split-window method described by Zhengming Wan & Dozier (1996) and filtered with the MODIS Cloud Mask products (MOD35 L2).

The meteorological data include wind speed (U) and near-surface air temperature (T_a) at the reference height of 2.7 m which were derived from planetary boundary layer (PBL) tower (30°48'53.44"N 90°47'49.72"E, green star in Figure 3-1) installed by the Nam Co Monitoring and Research Station for Multisphere, which was established by the Institute of Tibetan Plateau Research, Chinese Academy of Sciences (Ma et al., 2014). The wind speed and near-surface air temperature are measured at 05:00 (UTC) which is corresponding to the acquisition time of S2 data.

4. METHODOLOGY

4.1. Flowchart of methodology

Figure 4-1 showed the overview of this study. Apparently, this study divided into three parts.

The first part concentrates on validating the 2SeaColor model by the in-situ data. Remote sensing reflectance (R_{rs}) was inputted to the 2SeaColor model and then produced the K_d . Further, compared K_d produced by 2SeaColor model to K_d from in-situ data, consequently, the 2Seacolor model was validated by the in-situ measurements.

The second part focuses on dealing with the Sentinel 2 images and applying the 2SeaColor model to calculate the K_d of Namtso Lake. In addition, the validated 2SeaColor model applies to the Sentinel 2 images to produce the K_d map over Namtso Lake. Certainly, the validation of K_d map estimated by the combination of Sentinel 2 and the 2SeaColor model by the in-situ measurements could also be performed.

The third part is trying to establish a relationship between K_d and H to test the physical mechanism that how K_d impacts on H . This step achieved by first investigating the correlation between K_d and lake surface temperature (LST). Next, utilising the wind speed (U) and near-surface air temperature to calculate the H . At last, the spatial and temporal patterns were analysed between K_d and H .

K_d in this context specifies the K_d at a wavelength of 490 nm, namely $K_d(490)$. Because K_d as an apparent optical property (AOP) determined by such factors as viewing illumination geometries and inelastic scattering, thus, K_d is not constant with depth. However, as long as K_d at the adopted wavelength (490 nm), the effect exerted by these factors are too small to consider compared to the overall measurement errors (Zhang & Fell, 2007).

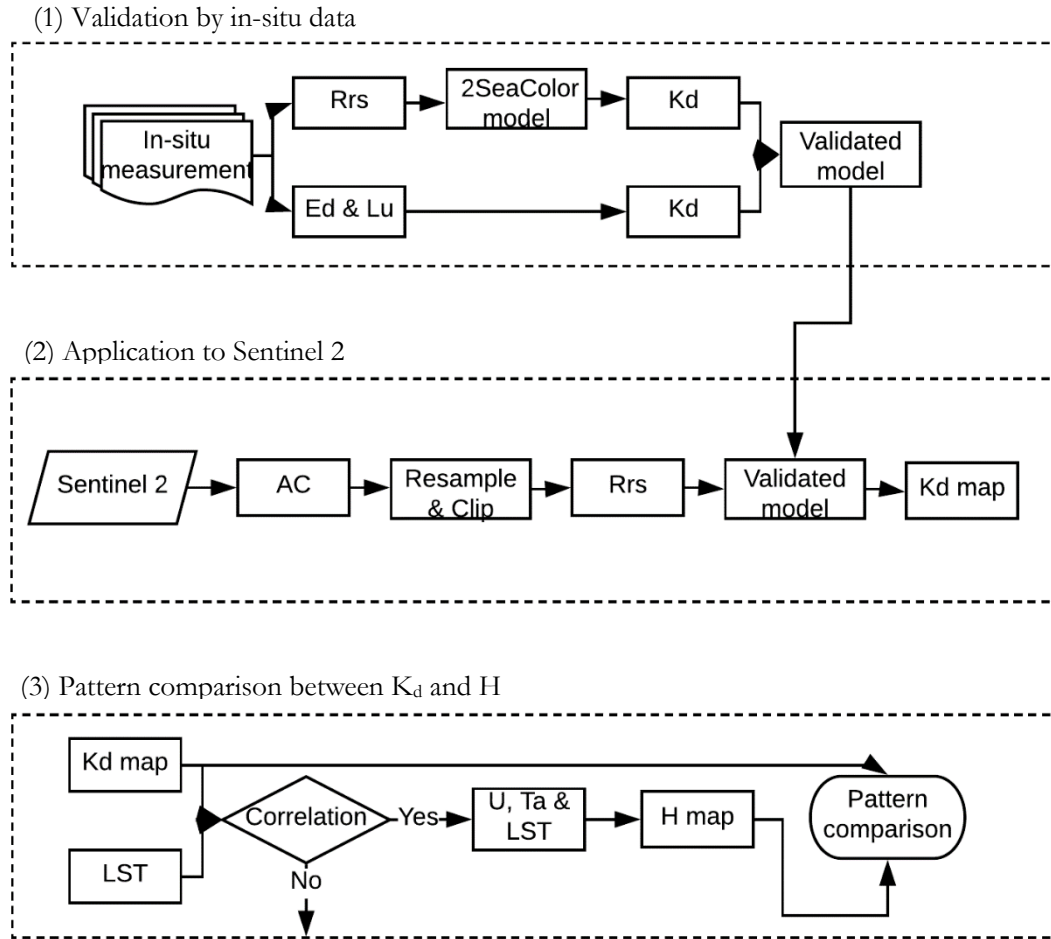


Figure 4-1 The flowchart of this study.

4.2. Models description

The 2SeaColor model is a two-stream remote sensing model proposed by Salama & Verhoef (2015). This model gives the solution of two-stream radiative transfer equation. The solution includes the forward formulation which connected R_{rs} to IOPs as well as the inversion scheme which is used for calculating K_d from IOPs.

4.2.1. Forward formulation

The forward formulation simulated the attenuation process using the first order radiative transfer equation(RTE) inside the water column for different components of irradiance, i.e. E_{ds} is the downwelling direct irradiance, E_{dd} is the downwelling diffuse irradiance, E_d is the total downwelling irradiance that equivalent to the sum of E_{ds} and E_{dd} , E_u is the upwelling irradiance. Also, the solution of the RTE was given. Therefore, the function between K_d and R_{rs} was derived. The following part presented the solution of RTE in the water column given by Salama & Verhoef (2015).

4.2.1.1. First-order differential radiative attenuation process inside the water column: mathematical implementation

The attenuation process of incident light within a water column characterised by the interaction between the light and the water constituents. The interaction consists of absorption and scattering. The absorption coefficient a and the backscattering coefficient b_b normally represent the optical properties of the water body. Figure 4-2 explicated the forward and backward scattering of a water molecule.

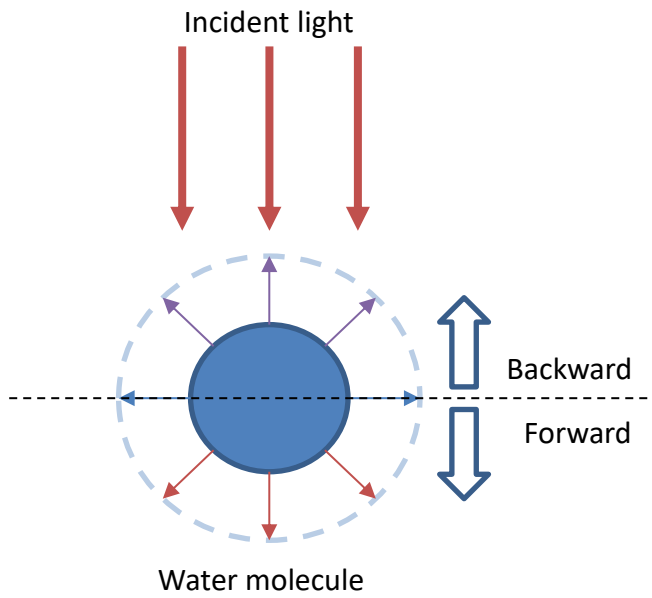


Figure 4-2 The scattering of a water molecule.

The radiative transfer equation described below (Duntley, 1942; Duntley, 1963):

$$\left. \begin{aligned} \frac{dE_{dd}}{dz} &= -s'E_{ds} + \alpha E_{dd} - \sigma \\ \frac{dE_u}{dz} &= sE_{ds} + \sigma E_{dd} - \alpha E_u \end{aligned} \right\} (1)$$

where k, s', s, α , and σ are the attenuation coefficients for different irradiance components. These components are listed in the Table 4-1 below.

Table 4-1 The coefficients description in the attenuation process.

Coefficients	Definition	Equation
k	The extinction coefficient m^{-1}	$k = c/\mu_s$
s'	Forward scattering for direct sunlight	$s' = b_f/\mu_s$
s	Backscattering direct for direct sunlight	$s = b_b/\mu_s$
α	The diffuse extinction coefficient	$\alpha = 2a + 2b_b$
σ	The diffuse backward scattering coefficient	$\sigma = b_b$
c	The extinction coefficient	$c = a + b$
μ_s	Cosine of solar zenith angle beneath the water	$\mu_s = \cos \theta_s$

The diffuse attenuation coefficient, K_d , for the direct and diffuse light was described by the following differential equation as:

$$K_d = \frac{1}{E_d} \frac{dE_d}{dz} \quad (2)$$

According to the solution of Eq.(1) given by Salama & Verhoef (2015), the function was shown below.

$$K_d = \frac{((k - s')E_{ds} + \alpha \cdot E_{dd} - \sigma \cdot E_u)}{E_d} \quad (3)$$

where

$$E_d = E_{dd} + E_{ds} \quad (4)$$

The r_∞ and r_{sd}^∞ are the bi-hemispherical reflectance for the semi-infinite medium and the directional-hemispherical reflectance of the semi-infinite medium. It is given by:

$$r_\infty = \frac{x}{1 + x + \sqrt{1 + 2x}} \quad (5)$$

$$r_{sd}^\infty = \frac{\sqrt{1 + 2x} - 1}{\sqrt{1 + 2x + \cos \theta_s}} \quad (6)$$

where $x = \frac{b_b}{a}$.

Therefore, the K_d was characterized by the IOPs. In addition,

$$R(0) = \frac{E_u(0)}{E_d(0)} = \frac{r_\infty \cdot E_{dd}(0) + r_{sd}^\infty \cdot E_{ds}(0)}{E_d(0)} \quad (7)$$

described the irradiance reflectance just beneath the water surface ($R(0)$). And then the $R(0)$ converted to the R_{rs} just above the water (Mobley, 1994):

$$R_{rs} = \frac{0.52R(0)}{Q - 1.7R(0)} \quad (8)$$

where Q is the Radiance-irradiance transfer coefficient which equals 3.25 in steradian (sr) under sunny conditions (Lee et al., 2002).

Hereafter, the function between R_{rs} and K_d was established.

4.2.1.2. Forward scattering of suspended particles

The suspended particles normally present a peaked forward scattering which is different from the water molecules. The schematic diagram of the suspend particulate showed in Figure 4-3. In general, the reflectance only related to the x which equals $\frac{b_b}{a}$. This would imply that the forward scattering is not taken into accounted the attenuation and backscattering. However, one can imagine that a proportion of the forward scattering still diffused and attenuated. Therefore, the 2SeaColor model consider the forward scattering component as a non-scattered flux in the attenuation process through similarity transformation (Hulst, 1981).

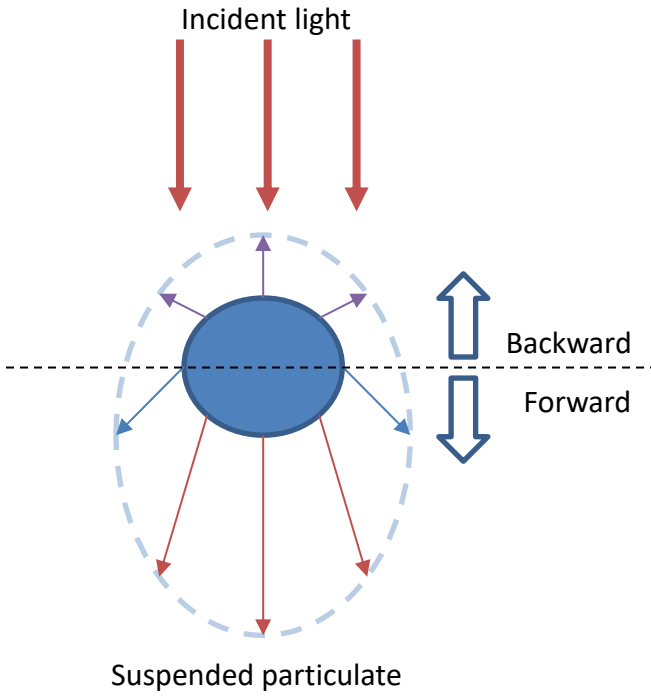


Figure 4-3 The scattering for a suspended particle.

4.2.2. Inversion scheme

The original 2SeaColor model proceeds through the assumption of the water molecule are the only contributor to absorption of incident light in a water column within Near Infrared (NIR). Meanwhile, if x was obtained through the relationship of R_{rs} and x , the b_b at NIR can be calculated. The b_b values at shorter wavelengths then obtained by bio-optical model. Therefore, a can be calculated from the b_b and x and thus, only backscattering coefficient should be parameterized. Recently, this model improved by Yu et al. (2016) using a parameterization of (Salama, Dekker, Su, Mannaerts, & Verhoef, 2009; Salama & Shen, 2010). Instead of parameterising the b_b , the improved 2SeaColor model parameterised the absorption coefficient of chlorophyll (α_φ) and combination of CDOM and non-algae (α_{dg}). The inversion scheme (Figure 4-4) started by firstly inputting the initial values. Subsequently, the spectral optimization was employed to simulate the R_{rs} through a nonlinear curve fitting based on the calculation of the minimum sum of squared differences. The parameterization showed below.

$$b_b = b_{bp}(\lambda_0) \left(\frac{\lambda_0}{\lambda}\right)^Y \quad (9)$$

$$\alpha_\varphi(\lambda) = \alpha_0(\lambda) + \alpha_1(\lambda) \ln\left[\left(\alpha_\varphi(440)\right)\right] \alpha_\varphi(440) \quad (10)$$

$$\alpha_{dg}(\lambda) = \alpha_{dg}(\lambda_0) e^{-S(\lambda-\lambda_0)} \quad (11)$$

where Y is the spectral slope of suspended particulates, and S is the spectral slope of the combination of CDOM and non-algae. Note Y is ranging from 0.3 to 1.7 (Lee, Du, et al., 2005). S is ranged between 0.011 and 0.019 nm^{-1} and an average value of 0.015 nm^{-1} is adopted in this study (Lee et al., 2002).

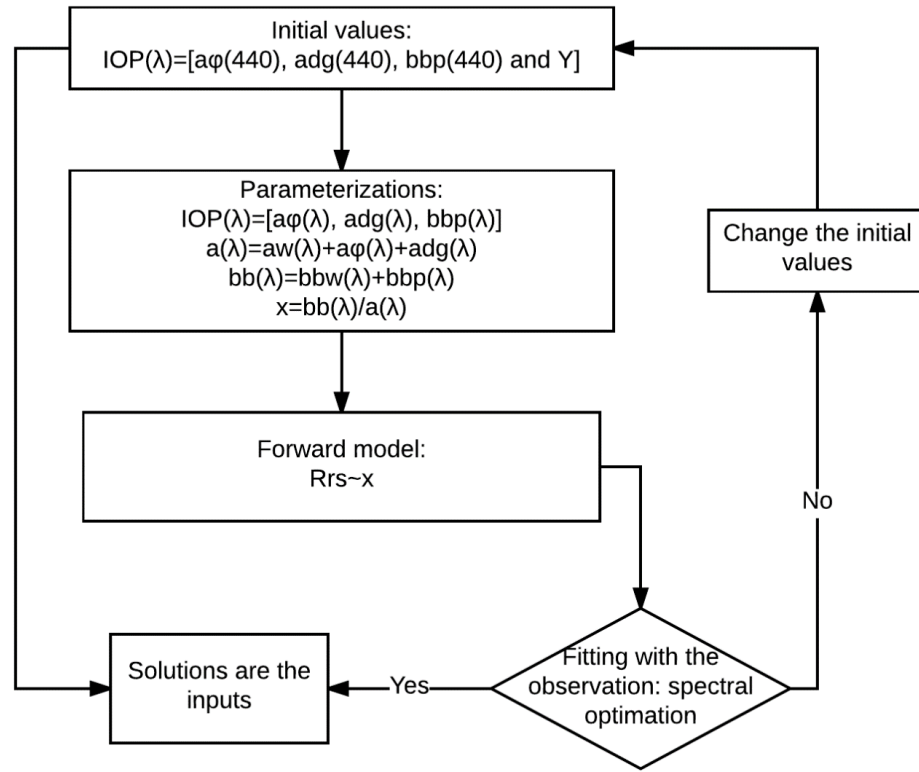


Figure 4-4 Inversion scheme of 2SeaColor model.

4.3. Atmospheric correction (AC) for Sentinel 2 data

AC for the coastal, transitional, and inland water application is a challenge due to the average ocean colour AC algorithms normally neglect surface level change, adjacency effects, and non-Lambertian surface reflection. Whereas iCOR and Alcolite are the state-of-the-art AC algorithm specify application of water which released on 8th of August 2017 and 18th July 2017, respectively. These two AC algorithms are going to be unfolded sequentially.

iCOR was originally designed for the airborne hyperspectral imagery. iCOR perform AC in following steps: (1) identify the water and land pixels, and the land pixels are used for the generation of AOT, (2) adjacency correction performed by SIMEC (Similarity Environment Correction), and (3) MODTRAN 5 (Berk et al., 2006) Look Up Tables (LUT) was used to perform the AC. The strength of iCOR is that it can recognize if a target pixel is a water or land and then performs a dedicated correction (Sindy Sterckx et al., 2015). In addition, the extra module, SIMEC (Similarity Environment Correction), which can remove the contamination of water pixels from the light of adjacency land and vegetation pixels (S Sterckx, Knaeps, Kratzer, & Ruddick, 2014). Three output files of iCOR contain: (1) all the spectra at 60m spatial resolution, (2) only bands with originally 20m spatial resolution and (3) only bands with originally 10m spatial resolution. More information could be found in the iCOR manual: http://ec2-54-149-255-197.us-west-2.compute.amazonaws.com/icor/manual/iCORpluginUserManual_v1.8.pdf.

Alcolite is an AC algorithm which can provide simple and fast processing for the Landsat 8 and S2 data. Alcolite execute atmospheric correction in two steps: (1) after Rayleigh scattering correction using the 6SV code (Vermote et al., 2006) to generate the LUT and (2) an aerosol correction based on the assumption of black SWIR bands over water due to the pure water molecules absorption and multiple scattering aerosol reflectance spectra (Vanhellemont & Ruddick, 2016). The resolution of output images is user-defined. It is worthy to mention that the Alcolite is a very powerful algorithm which can produce the product of, i.e. R_{rs} ,

chlorophyll-a concentration, SPM, turbidity, Quasi-Analytical Algorithm (Lee, Darecki, et al., 2005) which including IOPs and K_d .

In this paper, the 10m and 60m resolution outputs of AC algorithms were used to compare to the AC algorithm performance. Besides, this paper also evaluates the influence of different resolution to the AC accuracy. The nearest neighbour of up-sampling (interpolation) method and down-sampling (aggregation) method was adopted. The finer resolution product, 10m, allows more information of image is presenting and the coarser resolution product, 60m, provides a shorter processing time. Therefore, these two resolution products which have the best performance was selected for computing K_d .

4.4. Data analysis and accuracy assessment

To illustrate the performance of these models, there are four statistical parameters are planning present for the retrieved K_d (490) from the model result and known K_d (490) from in-situ data. The five statistical parameters are the root mean square error (RMSE), mean of absolute relative-differences (rMAD), slope and intercept of the linear regression as well as the square of correlation coefficient R^2 . The RMSE and rMAD expressed as:

$$RMSE = \sqrt{\frac{\sum (derived - known)^2}{N}} \quad (12)$$

$$rMAD = \sum \frac{\left| 1 - \frac{derived}{range} \right|}{N} \times 100\% \quad (13)$$

where N is the number of the observations. The slope and intercept are computed by model-II (Laws, 1997) regression. Clearly, for the perfect goodness-of-fit between retrieved and known K_d (490) should have RMSE=0, rMAD = 0, slope = 1, intercept = 0 and $R^2 = 1$.

It is inevitable that validation of the K_d map produced by application of best model from Sentinel 2. The accuracy assessment also represents the four statistical parameters.

4.5. Verification by Case 2 Regional Coast Colour (C2RCC) algorithm

The 2SeaColor model was verified by the C2RCC algorithm. Doerffer & Schiller, (2007) pioneered the development of the C2RCC algorithm for MERIS using the neural network technique. The C2RCC algorithm performed the AC and derived IOPs based on over five million cases of water types that generated by neural networks. The C2RCC also gives the K_d at the wavelength of 489 nm that employed in this thesis to verify the 2SeaColor model. C2RCC is applicable for all the ocean colour sensors, i.e. Sentinel 3 OLCI, Sentinel 2 MSI, MERIS and SeaWiFS. C2RCC was widely validated by numerous of researchers, and it can access by ESA' s Sentinel toolbox, SNAP. The detail of the atmospheric correction and IOPs retrieval is illustrated by Brockmann et al., (2016).

4.6. The correlation analysis for K_d and H

From a physical view, the K_d impacts on the LST, and consequently on H. However, it is hard to observe the impactation. Therefore, the correlation analysis between K_d and H performed by firstly, correlating the K_d and MODIS LST product, and secondly by analysing the spatial dependency relationship between K_d and H.

4.6.1. The temporal correlation analysis for K_d and LST

The LST product was georeferenced and projected to share the same geographical and projection coordinate with the K_d map produced by 2SeaColor model. Also, the values of not a number (NaN) in the LST product was masked out. In addition, the correlation analysis executed only for the water pixels, thus, the K_d values ranging from 0 to 2 m^{-1} were selected to define the water pixels.

The correlation coefficient, R, was computed by using

$$R = \frac{\sum_m \sum_n (A_{mn} - \bar{A})(B_{mn} - \bar{B})}{\sqrt{(\sum_m \sum_n (A_{mn} - \bar{A})^2)(\sum_m \sum_n (B_{mn} - \bar{B})^2)}} \quad (14)$$

where A and B are the matrices (images) that share the same size, i.e. m rows and n columns (pixel location). Besides, \bar{A} , and \bar{B} are the mean value in A and B. Hence, the basic operator what Eq. (14) calculated is, the difference, for every water pixel location, between the value in that pixel and the mean value of the whole image (Figure 4-5). Besides, the denominator presents a kind of normalization where the pixel value difference within every individual image. In summary, R, in this context, showed the overall correlation of all pixels regardless the spatial aspect. Therefore, R can indicate the relationship of two images with respect to temporal variations.

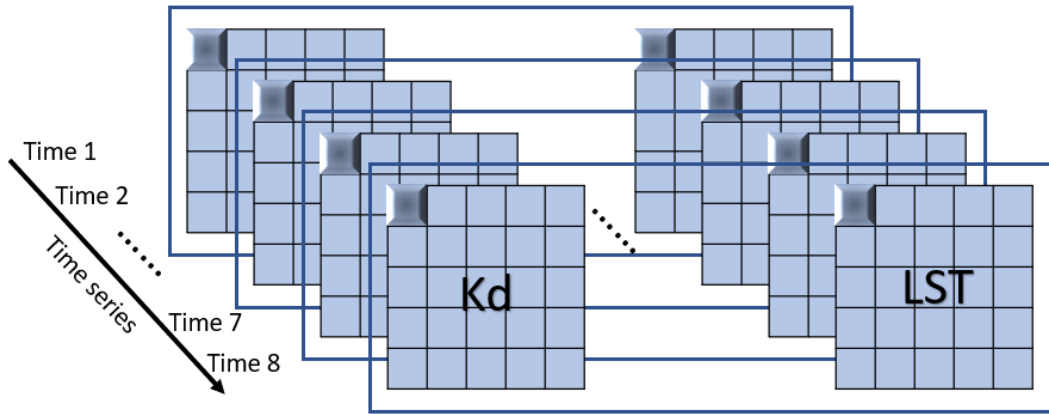


Figure 4-5 Schematic diagram of temporal correlation.

4.6.2. The spatial correlation analysis for K_d and LST

The spatial correlation analysis computed the correlation coefficient for every water pixel of the LST daytime products (6th December.2016, 27th September.2017, 17th October.2017, and 22nd October.2017) and corresponded K_d maps (Figure 4-6). Therefore, the result is a map of correlation coefficient which can present the spatial relationship.

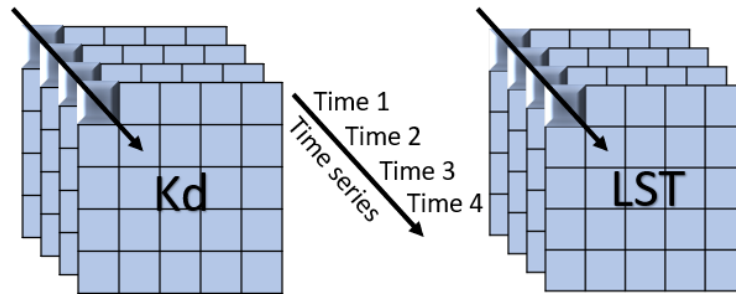


Figure 4-6 Schematic diagram of spatial correlation.

4.6.3. The correlation analysis for K_d and H

H was calculated as:

$$H = C_p \rho_a C_H U (T_s - T_a) \quad (15)$$

where C_p ($1009 \text{ J} \cdot \text{kg}^{-1} \cdot \text{K}^{-1}$ at $10 \text{ }^\circ\text{C}$) is the specific heat of air, ρ_a ($0.73 \text{ kg} \cdot \text{m}^{-3}$ at TP) is the air density, C_H is the bulk transfer coefficient which adopt $1.834 \cdot 10^{-3}$ at reference height above the lake according to Kondo, (1975), and U is the wind speed. T_s and T_a are the lake surface temperature and air temperature obtained from PBL tower at reference height, respectively.

The correlation coefficient for the K_d and H was calculated only for the daytime LST time series because this correlation coefficient was based on a pixel which could induce turbulence if the entire time series was counted.

5. RESULTS

5.1. Remote sensing reflectance and K_d from in-situ measurement

The remote sensing reflectance (R_{rs}) and the diffuse attenuation coefficient (K_d) calculated from field data (E_d and L_u) are presented in Figure 5-1. The peak in R_{rs} (Figure 5-1 (a)) can be found at blue-green band region. On the contrary, the extremely low values of R_{rs} were caused by the intense absorption of pure water molecules in the red and NIR (Majozi, Suhyb, Bernard, Harper, & Ghirmai, 2014) (Ruddick, De Cauwer, Park, & Moore, 2006). Looking at the K_d (Figure 5-1 (b)), the valley at blue-green band represent the attenuation of incident light is not strong, while the peak in Figure 5-1 (b) at NIR band also showed the consistent result with R_{rs} as almost all incident light was absorbed at NIR band.

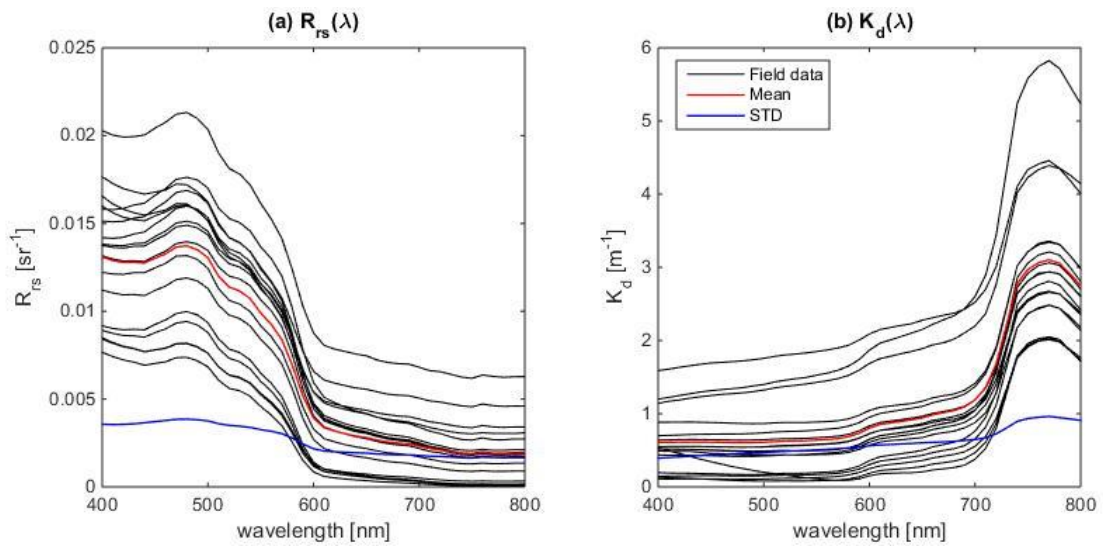


Figure 5-1 Field measurements of R_{rs} and K_d spectrum curves (black) with their mean (red) and standard deviation (blue) values.

Table 5-1 showed the mean values and standard deviations for K_d as an auxiliary for understanding the spectrum. Therefore, these spectrum features suggested most of the sites of water are relatively clear without so much presence of phytoplankton, SPM, and CDOM. This preliminary speculation is similar to the result of the previous research (Yong, Liping, Junbo, Jianting, & Xiao, 2012).

The R_{rs} spectrum curves highly fluctuate over the visible and near-infrared area. In addition, the K_d spectrum curves also showed high variation with respect to magnitude and shape. Variations of these spectrum curve mainly due to the undulating weather condition which means high frequency switching of cloudy and clear skies at the time the spectra were collected. Besides, the optically important water constituents spatial and temporal distribution also accounts for the fluctuations. As a matter of fact, the underwater topography and river supply may also exert an unexpected effect on the R_{rs} and K_d variations.

Table 5-1 The average values (mean) and standard deviations (STD) for the R_{rs} and K_d of selected wavelengths over Namtso Lake.

Wavelength	400	450	500	550	600	650	700	750	800
K_d _Mean	0.61	0.61	0.61	0.64	0.80	0.94	1.19	2.97	2.75
K_d _STD	0.39	0.44	0.47	0.51	0.56	0.60	0.65	0.93	0.91

5.2. Validation for K_d retrieved by 2SeaColor model

5.2.1. Validating K_d by in-situ measurements

2SeaColor model (Salama & Verhoef, 2015) are used to estimate the K_d of Namtso Lake. Figure 5-2 showed the scattering plot of derived K_d (490nm) from the model against known K_d (490nm) from field measurements. The only input of 2SeaColor model is the remote sensing reflectance from field measurements.

The K_d produced by 2SeaColor possesses a relatively large deviation in turbid water where $K_d > 0.2 \text{ m}^{-1}$ (I. Zhang & Fell, 2007). Besides, the model underestimated the K_d when the K_d values greater than 0.5 m^{-1} as the slope ($=0.61$) is more than 20% off unity. Looking at the R^2 ($=0.765$) and the relative error, rMAD ($=12.32\%$), which demonstrate the 2SeaColor model is relatively reliable. Besides, the intercept ($=0.07$) from the linear regression between modelled and known K_d of 2SeaColor model is close to zero. The intercept represented a small linear offset between the modelled K_d and known K_d . Therefore, it can conclude from above results the 2SeaColor model performs acceptably despite the underestimation.

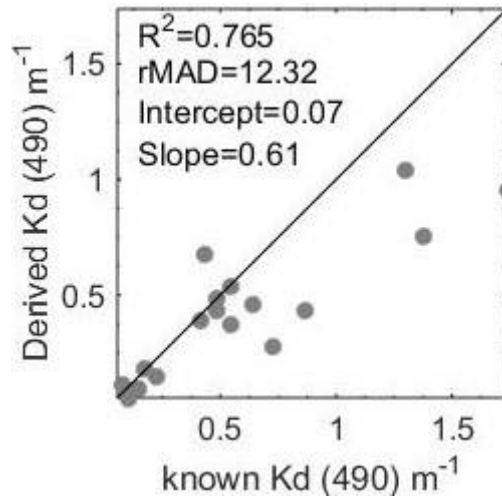


Figure 5-2 Derived K_d (490nm) from 2SeaColor model against known K_d (490nm) from field measurements.

5.2.2. Validating K_d by Convolved in-situ measurements

The instrument spectral response functions (SRFs) or relative spectral responses describe the quantum efficiency of an instrument at specific wavelengths over the range of a spectral band (Fleming, 2006). Therefore, the R_{rs} measured by TriOS Ramses sensors (in situ data) should be matched up the S2 MSI, namely convolution. The convolution achieved by the following formula

$$R_{rs(i)(convolved)} = \frac{\int_{\lambda_1}^{\lambda_2} (R_{rs(j)(in-situ)}(\lambda) * SRFs_i(\lambda)) d\lambda}{\int_{\lambda_1}^{\lambda_2} SRFs_i(\lambda) d\lambda}$$

where i is the number of bands of Sentinel 2, j is the site's number of in situ data as well as the λ_1 and λ_2 are adopt 400nm and 800nm thereby.

Figure 5-3 showed the validation of 2SeaColor model by convolved in-situ R_{rs} measurements. Obviously, the 2SeaColor model performed better after convolution. But K_d is also dispersed as increasing of the known K_d . The R^2 was slightly higher than the result of field modelled. The rMAD and slope were diminished. Also, the almost accordance slope was given by 2SeaColor model after convolution. In summary, the convolution provided an overall better result for the modelling.

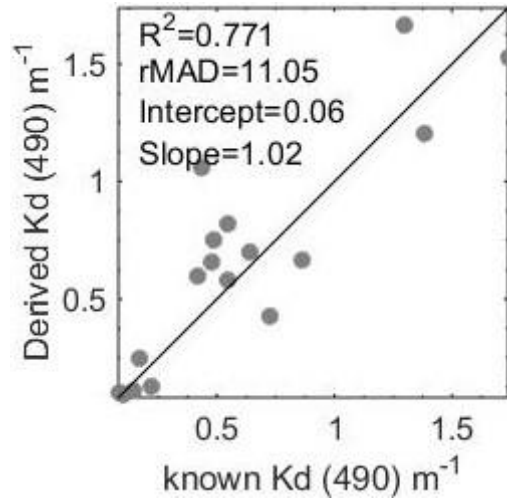


Figure 5-3 Derived K_d (490nm) from 2SeaColor model against known K_d (490nm) from convolved field measurements.

5.3. Estimating K_d from Sentinel 2 image

In order to further illustrate the potential of the 2SeaColor model for remote sensing K_d , the Sentinel 2 data were tested to validate the applicability. The processing of Sentinel 2 proceeds to the atmospheric correction. Simultaneously, convolving the in situ remote sensing reflectance to Sentinel 2 MSI spectra. After convolution, the newly produced in situ remote sensing reflectance data transfer the view of TriOS Ramses sensors to the view of Sentinel 2 MSI. Sequentially, mapping K_d by applied 2SeaColor model to atmospheric corrected Sentinel 2 image. At last, validating the map of K_d generated from 2SeaColor model by the in situ K_d measurements.

5.3.1. Atmospheric correction (AC) for Sentinel 2 image

The weather was cloudy when collecting the field data which resulted in the large errors occurred for both iCOR and Alcolite algorithms. However, iCOR has better performance for some of field data sites.

The comparison of iCOR and Alcolite AC algorithms in 10m and 60m resolution of one site showed in Figure 5-4. Blue lines represent R_{rs} from iCOR algorithm (the output of iCOR is water leaving reflectance, and thus it has to transfer to R_{rs} divided by pi hereby). Red lines stand for R_{rs} from the Alcolite algorithm. And black is the convolved field measured R_{rs} data. Additionally, solid lines represent 10m spatial resolution while dash lines stand for the 60m spatial resolution. The statistical parameters are shown in Table 5-2 for an insight of the assessment of AC algorithms.

Apparently, the spectra of iCOR in 60m spatial resolution is much closer than the others to the field measurements from the Figure 5-4. And only the iCOR in 60m spectra describes the trend of 443nm and 490nm ($R_{rs}(443) > R_{rs}(490)$) in the same way with the in situ R_{rs} . Besides, the R^2 represents the strength of correlation between field data and AC results regarding shape, and the iCOR in 60m have the largest value means the iCOR in 60m own the strongest relationship with the field data compared to the others. With respect to RMSE and rMAD, the spectra of iCOR in 60m also possesses the smallest values (RMSE=0.0019. rMAD=19.2977%). The rMAD of iCOR in 10m and Alcolite in 10m are excess 100% which signifies the R_{rs} values between rMAD of iCOR in 10m as well as Alcolite in 10m and field measured are not in the same magnitude. Therefore, the iCOR at 60m was adopted to perform AC.

It has to be mentioned that iCOR in 60m AC algorithm is not performed as good as this one site for all the field data, it is considered, however, adequate for this study.

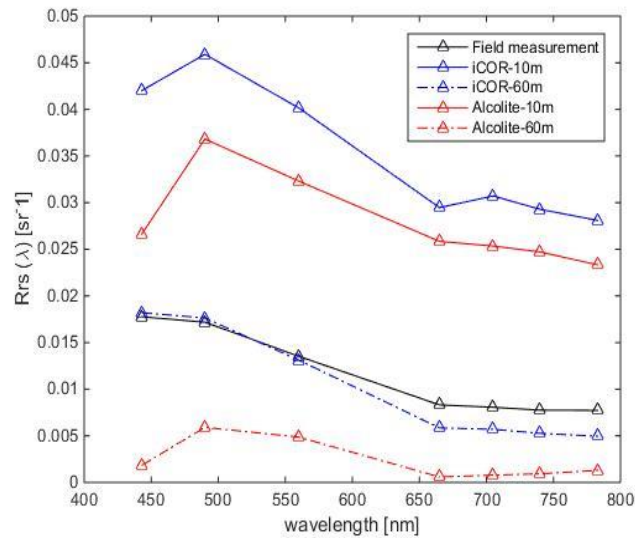


Figure 5-4 Assessment of AC algorithms with the convolved field measured R_{rs} data in 10m and 60m spatial resolutions.

Table 5-2 Statistical parameters of the iCOR and Alcolite AC algorithms in 10m and 60m spatial resolutions.

	iCOR_10	iCOR_60	Alcolite_10	Alcolite_60
R^2	0.94	0.99	0.55	0.51
RMSE	0.0238	0.0019	0.0167	0.0097
rMAD	225.36	19.30	164.17	81.95

5.3.2. Mapping K_d by 2SeaColor model

Figure 5-5 depicted the K_d maps at the wavelength of 490 nm from October to December of 2016 and 2017 of Namtso Lake. It must mention that the easily observed discrete horizontal line was created by mosaicking in Figure 5-5 (a) and (e). Also, the relatively conspicuous strip area was the S2 camera trace for all the images showed in Figure 5-5. Besides, there were several small abnormal areas in 28th Oct.2016, 6th December.2016 and 16th December.2016 caused by clouds. Thus, these three effects should ignore when one analysing the spatial and temporal patterns of K_d .

The spatial characteristics could be observed, as nearshore waters presented a high K_d value, particularly at the north and west of the lake, whereas, the offshore waters showed a much lower K_d value. The values of K_d on 28 October 2016 (Figure 5-5 (b)), however, exhibited an inverse spatial pattern, as the high values can be found in the middle of the lake, while, only the west of the lake presented a low K_d value. Besides, the K_d on 27 September 2017 (Figure 5-5 (e)) also showed a different pattern that K_d is high except the south of the lake.

As for the temporal pattern of K_d , there are no enormous variations within the whole time series regardless the Figure 5-5 (b) and Figure 5-5 (e). However, one can conclude that K_d in December is lower than the October if neglects the data limitation.

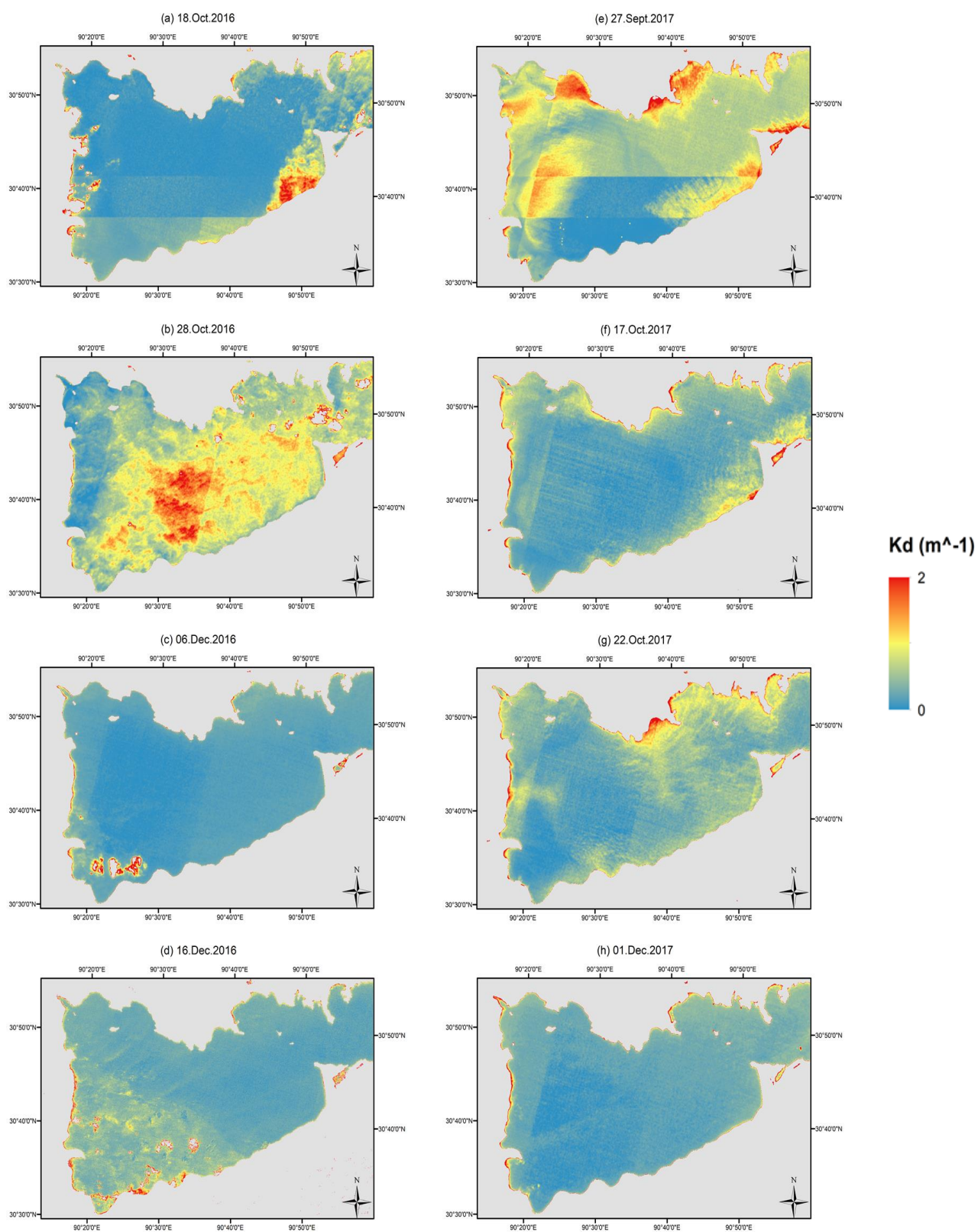


Figure 5-5 K_d (490nm) maps estimated by 2SeaColor model using atmospheric corrected S2 data for Namtso Lake on eight days: (a) 18th Oct. 2016, (b) 28th Oct.2016, (c) 6th Dec.2016, (d) 16th Dec.2016, (e) 27th Sept.2017, (f) 17th Oct.2017, (g) 22nd Oct.2017, and (h) 1st Dec.2017.

5.4. Verification

The statistic variables were K_d for C2RCC and 2SeaColor models on three days were shown in Table 5-3. The field measurement also shown as the indicator of model performance. Apparently, according to the mean values of C2RCC and 2SeaColor on the day of 28th Oct 2016, the 2SeaColor has a better performance since it is closed to the mean value of the field data, while the mean values of C2RCC are smaller than the 2Seacolor's on all the three days which means the C2RCC could underestimate the K_d . In addition, the stand deviations of 2SeaColor model are much greater than C2RCC's could indicate the K_d produced by 2SeaColor model is more dispersion. The stand deviation and dynamic range (DR) of 2SeaColor, however, closed to the field data on 28th Oct 2016 represented K_d of 28th Oct 2016 and field data share the similar range.

Overall, the 2SeaColor has better performance while the C2RCC is underestimated the K_d .

Table 5-3 The statistic variables of K_d for C2RCC and 2SeaColor models on three days. DR represents dynamic range (N=10).

	28 th Oct.2016			15 th May.2017			22 nd Oct.2017		
Statistics	Mean	STD	DR	Mean	STD	DR	Mean	STD	DR
C2RCC	0.106	0.038	0.129	0.162	0.031	0.118	0.095	0.017	0.065
2SeaColor	1.069	0.445	1.366	2.344	0.915	2.524	0.442	0.142	0.580
Field data	Mean: 0.752, STD: 0.471, DR: 1.151 collected on 25th May.2017.								

5.5. K_d and sensible heat flux (H)

5.5.1. The temporal correlation analysis for K_d and LST

The relation between K_d and LST with respect to temporal variation was quantified by the correlation coefficient (R) showed in Figure 5-6. R took the contributions for all the pixels into consideration regardless the spatial distribution, thus, it represented the temporal correlation ignored the spatial influence. One can observe that R contained both positive and negative values from Figure 5-6. This inconsistency is able to attribute to the replacement of night-time LST product because night-time LST presented an inverse behaviour compared to the daytime LST, i.e. the lake surface temperature is lower than the land temperature at daytime while it is opposed at night time. Besides, the only R of 22nd October 2017 was greater than 0.5, while others are relatively low. This may imply lake surface temperature is not determined by diffuse attenuation coefficient exclusively, further, it is hard to isolate the effect of light attenuation to the lake surface temperature. In addition, the low correlation coefficients could also attribute to (1) the different acquisition time between S2 and MODIS, (2) the algorithm of LST computation, since there is no in-situ lake surface temperature was collected in the Namtso Lake, thus, the LST data from MODIS was not validated.

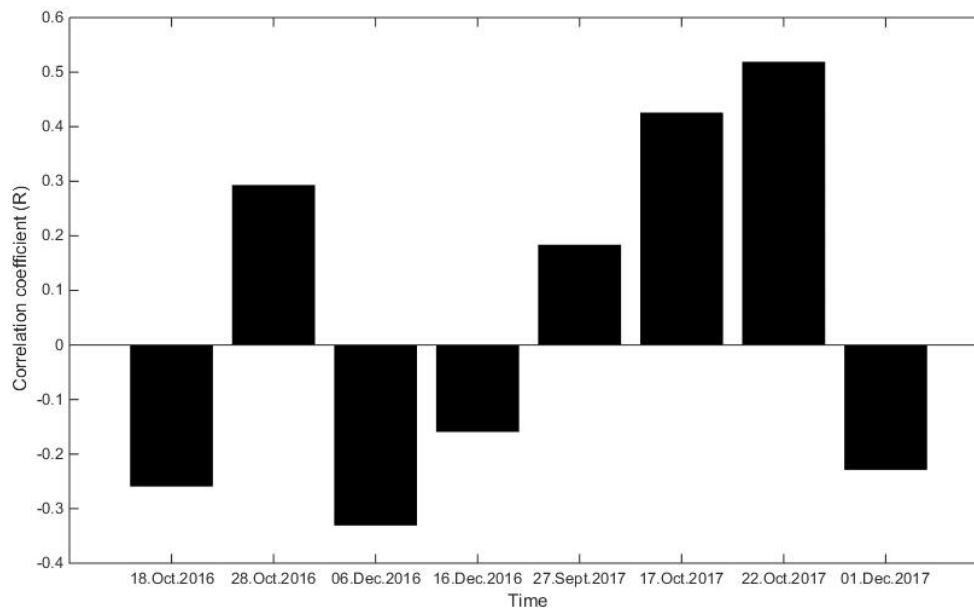


Figure 5-6 The correlation coefficients between K_d and LST.

5.5.2. The spatial correlation analysis for K_d and LST

Every pixel value in correlation (r) map (Figure 5-7) were computed by two columns of data as (1) the pixel value of LST for all the daytime series (2) the pixel value of K_d for all the same time series and location with LST. Therefore, the correlation map presented the spatial characteristics of the relationship between K_d and LST. Apparently, it is easy to observe that the most areas of the lake own a high correlation coefficient except the south of the lake. The correlation almost zero in the south of the lake indicated that the K_d and LST are almost uncorrelated. Besides, there is a small parcel presented a high negative correlation in the southwest part of the lake.

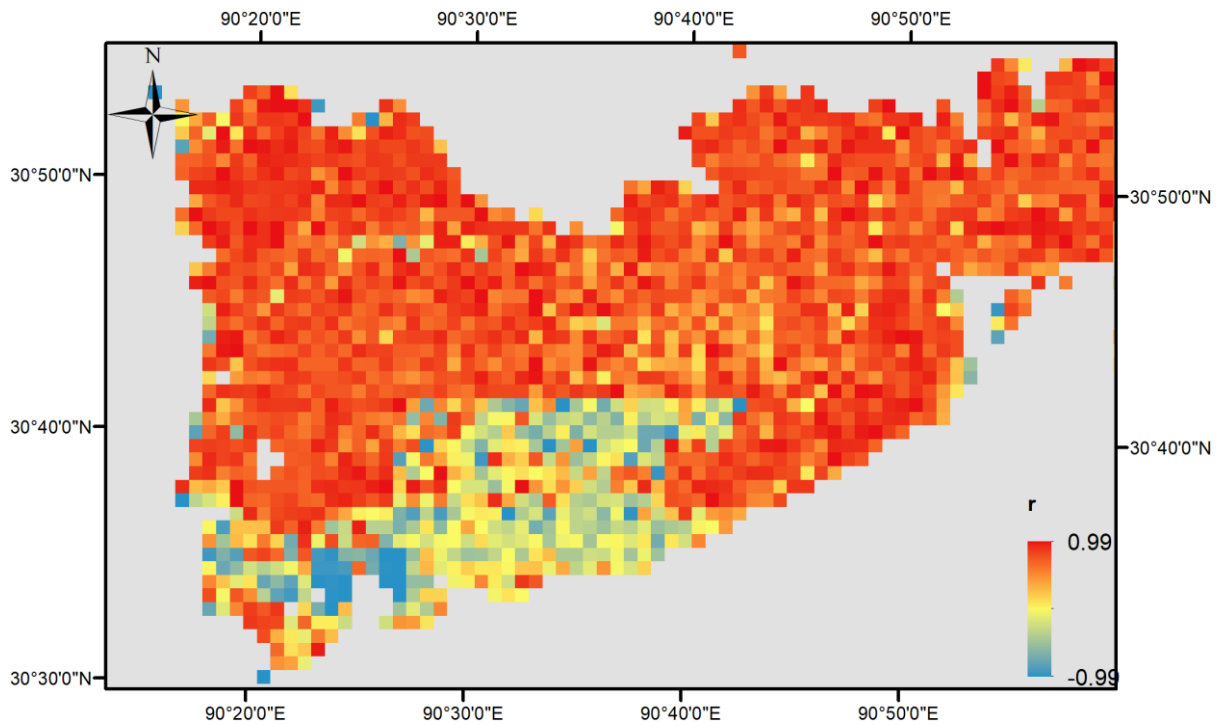


Figure 5-7 The correlation coefficient (r) map for K_d and LST.

5.5.3. The correlation analysis for K_d and H

According to the Eq. (15), the sensible heat flux (H) and the correlation coefficients were (C_o) computed and was shown in Table 5-4. The correlation coefficient for K_d and LST (T_s) at the single site, PBL tower site, is 0.93 which indicate that K_d and LST have a strong positive relationship, while the correlation coefficient for the K_d and H is -0.85 which present a strong negative relationship. The correlation coefficient for the K_d and the difference between T_s and T_a (ΔT) is -0.66, the correlation coefficient between the wind speed (U) and H is 0.98 indicated that the wind speed predominates the sensible heat flux.

Table 5-4 The meteorological data, computed H and the correlation coefficients.

	Date	U(m/s)	Ta(K)	Ts(K)	$T_s - T_a$ (K)	K_d (m^{-1})	H($W \cdot m^{-2}$)	Co_{K_d-Ts}	$Co_{K_d-\Delta T}$	Co_{K_d-H}	Co_{H-U}
Daytime	6 th .10.2016	7.6	271.2	277.6	6.5	0.23	64.9				
	27 th .09.2017	1.0	282.7	285.9	3.3	0.50	4.2	0.93	-0.66	-0.85	0.99
	17 th .10.2017	0.9	278.4	283.6	5.2	0.35	6.4				
	22 nd .12.2017	2.7	274.7	283.2	8.5	0.34	30.1				
Night time	18 th .10.2016	2.3	276.1	282.4	6.3	0.04	19.4				
	28 th .10.2016	2.6	269.0	278.9	9.9	1.15	33.9	-0.12	0.79	0.52	0.6
	16 th .12.2016	10.6	272.8	275.4	2.5	0.19	35.6				

6. DISCUSSION

In this study, the 2SeaColor model was employed to estimate the K_d over Namtso Lake. The model was validated by in situ data. Further, the sensible heat flux (H) was computed, sequentially, the correlation analysis was conducted between K_d and H.

6.1. Assessment of 2SeaColor model

6.1.1. Validation

It is found that 2SeaColor model using the convolved R_{rs} performed much better than before convolution. This is mainly because convolution averaged the error. The slight discrepancy of R_{rs} was enhanced when propagated to IOPs, i.e. absorption coefficient and backscattering coefficient, through the spectrum optimisation. The equations (Eq. (9) (10) (11)) employed by spectrum optimisation was an exponential function which leads to the enhancement of IOPs. The absorption coefficient (a) and backscattering coefficient (b_b) increased by 44.7% and 35.8% averagely for all the in-situ measurements. The ratio x of backscattering coefficient to the absorption coefficient present an ensemble effect of light attenuation, thus, x was reduced due to the increasing of IOPs. Therefore, it indicated that more energy of incident light was attenuated by the water constituents, consequently, K_d produced by 2SeaColor increased.

The significant improvement in terms of slope can be understood that the convolution plays a critical role in the K_d retrieval. Spectral response functions define the spectral band position and extent, thus, it is normally considered as the pivotal source of uncertainty and compatibility for different sensors (D'Odorico, Gonsamo, Damm, & Schaepman, 2013; Teillet, Fedosejevs, Thome, & Barker, 2007). Although the convolution is by no means affected the overall spectral shape of R_{rs} , it has a significant impact on K_d .

The impact also reflects that AC should be very careful to be treated (Wang, Son, & Shi, 2009).

This result showed the 2SeaColor model was stable and applicable to the alpine Lake Namtso using S2 data. Also, it was consistent with previous studies that validation of 2SeaColor model in Naivasha Lake (Suhyb Salama & Verhoef, 2015) and Yangtze estuary (Yu et al., 2016).

6.1.2. Verification

Basically, 2SeaColor model and C2RCC model have a different range of the estimated K_d which could mainly due the employed the totally different AC algorithm. The only input of the 2SeaColor model is the remote sensing reflectance that derived from AC, hence, AC is attributed to the enormous difference between the K_d estimated by 2SeaColor model and C2RCC model. In addition, the mean value and stand deviation of 2SeaColor on the 15th May 2017 in Table 5-3 is greater than the field data, which indicated on that day, the 2SeaColor model could overestimate the K_d . Therefore, it is concluded that both of the 2SeaColor model and C2RCC model are not given a very good agreement, while comparably, the 2SeaColor model explicated a better performance.

6.2. The spatial and temporal characteristics of K_d in Namtso Lake

The K_d is an apparent optical property that depends on the illumination-viewing geometry. Since 2SeaColor model takes into accounts the solar zenith angle, thus, solar zenith angle is not considered as a factor that affects the K_d variation. Besides, K_d is the quantification of the underwater light availability, and it is determined by the and IOPs of optically active water constituents. In general, typical optically active water constituents such as chlorophyll-a (Chl-a), dissolved organic matter (DOM), suspended particulate matter (SPM) mainly influence the K_d variability (Mobley, 1994; Liu et al., 2010; Cairo, Barbosa, de Moraes Novo, & do Carmo Calijuri, 2017). Morel & Antoine (1994) suggested K_d rises from the concentration of Chl-a caused by bio-optically induced radiative heating.

The geographical information explains the distribution of optically active water constituents in Namtso Lake. About 60 rivers flowing into the Namtso Lake and most of these rivers are small rivers. These small rivers distributed in the west and south of the lake (Wang et al., 2010). Additionally, Wang et al., (2010) indicated the large perennial rivers are drain into the western and eastern parts of the lake.

The underwater topography has an important effect on the SPM enrichment. Bathymetric survey was conducted to understanding the underwater topography features (Wang et al., 2009). There is a large deep flat area in the centre of the lake, and the deepest depth could reach 98.9m. Besides, the lake floor slope with a sharp gradient was found at the north and south of the lake where mountains are situated, while the west and east have a gentle slope where the alluvial fans are distributed caused by the large perennial rivers. Thus, it has a potential of SPM enrichment in Namtso Lake.

Liu et al. (2010) suggested that high Chl-a was found in the northern offshore water of Namtso Lake in September 2005. But the average value of Chl-a was $0.46 \mu\text{g}\cdot\text{L}^{-1}$ which are still low. Lami et al. (2010) indicated the concentration of pigments was increased during the recent years. It can attribute to the extended growing season of algae caused by climate warming. Nima et al. (2016) found that the concentration of Chl-a was very low ($0.1 \mu\text{g}\cdot\text{L}^{-1}$) although the sample was collected during the productive season, May to September.

To sum up, K_d in Namtso Lake is dominated by SPM rather than by the concentration of Chl-a. The northeast and the northwest of the lake showed a high K_d value. This is mainly because the sand and silt transported by the rivers were enriched in the northeast and northwest of the Namtso Lake. The sand and silt could view as the SPM which often explicit a strong forward scattering. The strong forward scattering considered as the non-scattering fluxes by a 2SeaColor model that results in the K_d increased. In fact, the K_d values are still low compared to other study areas (Lee, Du, et al., 2005; Zhang & Fell, 2007; Simon & Shanmugam, 2016) that indicate the Namtso Lake is a reasonable turbid alpine lake that K_d varied with time (Vollenweider, 1982; Nima et al., 2016).

As for the temporal pattern, due to Namtso Lake located in the TP which is known as extremely cold in winter, little activity of water, also phytoplankton (Calijuri, Dos Santos, & Jati, 2002) and suspended particulates was presented. Therefore, the K_d explicated a similar pattern of variation in December. In another hand, K_d in September and October, especially on the day of 28th of October 2016 presented a much greater spatial variation than the K_d in December. The greater spatial variations of K_d on 28th of October 2016 could attribute to the large ΔT value (9.9 K). It is reported that the largest ΔT appeared in the autumn and winter in Namtso Lake (Haginoya et al., 2009). Due to the significant difference between air temperature and water surface temperature, the deeper water is requested to exchange energy with the upper layer water in order to compensate the large difference between lake surface temperature and air temperature. This request leads to the enhancement of the stratification and convection of the upper layer of the lake. This result could compare to the study on the Labrador Sea (Wu et al., 2007) that the mixed-layer depth reduced by 20-50% after the external heating induced to the water body.

6.3. The relationship between K_d and H

Increased K_d represents more incoming solar radiation being attenuated by the upper layer of the water body (Giardino, Pepe, Brivio, Ghezzi, & Zilioli, 2001; Zhang et al., 2015; Chen, Zhang, Xing, Ishizaka, & Yu, 2017). The attenuated solar energy could result in the increasing of the water surface temperature. It is known that surface temperature is one of the factors that controlled the sensible heat flux. Previous studies (Wu et al., 2007; Wu, Platt, Tang, & Sathyendranath, 2008) demonstrated the bio-optically induced K_d variations impact on the water surface temperature. However, rare studies concentrated on the question: to what extent, the K_d dominate the LST or H? This study conducted the correlation analysis between K_d and LST for the whole Namtso Lake, also the correlation between K_d and H for one point of the Namtso Lake.

6.3.1. The temporal correlation analysis of K_d and LST

R , temporal correlation coefficient in this context, represents the correlation between instantaneous variables K_d and LST for all the pixels and for every single acquisition time of S2 and MODIS. Figure 5-6 indicates that it is not conclusive that the K_d and LST are correlated within the eight selected dates due to the low correlation coefficients. This result could attribute to (1) K_d and H are instantaneous variables, thus, different acquisition time of S2 and MODIS could lead to the uncorrelation, (2) R explicated the overall effect (refer to Eq.14) of the map of K_d and LST which could eliminate some interconnections between K_d and H. Additionally, the correlation coefficients of 17th and 22nd October 2017 are relatively high compared to other dates. The reason for the high temporal correlation coefficient needs more investigation. In summary, the K_d and LST are varied in these eight acquisition time, so the results are not enough to draw a conclusion.

6.3.2. The spatial correlation analysis of K_d and LST

The spatial correlation coefficients, r , represent the correspondence for every pixel between K_d map and LST map for the four daytime products. The result (Figure 5-7) of spatial correlation analysis showed K_d is significantly positively correlated with LST except for the south part of the lake. The result indicated that the K_d and LST shared the same pattern within the specified time series for the most part of the lake. The weak correlation at the south part of the lake could attribute that the values of K_d at the south of the lake on the 27th September.2017 was lower than the other three days. Besides, a small area with the extreme high negative correlation coefficient occurred in the bottom left corner on account of the clouds on the day of 6th December.2016. The edge of the clouds presents a much higher K_d values than the water due to the strong attenuation effect by the clouds, thus, the K_d of the edge of clouds was very high. The centre of the clouds is no value in the K_d map because the R_{rs} is too high to input to the 2SeaColor model.

Previous studies (Wu et al., 2008; Giardino et al., 2001; Wu et al., 2007) normally focus on how LST varied with K_d instead of the correlation analysis.

In summary, LST is the boundary that connects the turbulent air and the turbulent water. Generally, LST dependent on sensible heat flux that the LST air-water heat flux feedback is around $20 \text{ W} \cdot \text{m}^{-1} \cdot \text{K}^{-1}$ for the seawater (Hausmann, Czaja, & Marshall, 2016; Frankignoul, Czaja, & L'Heveder, 1998), considering, also, the high correlation between K_d and LST presented in Figure 5-7 that indicated K_d is related to H. However, solar radiation, wind speed, horizontal advection and stability of the water column also determined the LST (Emery & Yu, 1997). Therefore, one should consider not only the relationship between K_d and LST but also consider the other parameters of air-water interaction if one performs the correlation analysis between light attenuation and water surface temperature.

6.3.3. K_d and H

The correlation coefficients of environment variables among the air-water interaction are listed in Table 5-4 above. The correlation coefficients (K_d & T_s , K_d & ΔT , K_d & H and H & U) only calculate from the PBL site which site contains the meteorological data. The daytime correlation coefficients computed by the daytime LST products on 6th December.2016, 27th September.2017, 17th October.2017, and 22nd October.2017 as well as the corresponding K_d map produced by 2SeaColor model. The night time correlation coefficients were calculated in the same way. Table 5-4 showed the low coefficients of night time simply because the K_d and LST product is not acquired at the same time as K_d maps were acquired at daytime, but LST products were acquired at night time.

For daytime correlation coefficients, the significant negative correlation coefficient ($=-0.85$) between K_d and H indicated that an increase of K_d results in a decrease of H. This is mainly because when K_d increased, more energy was tapped in the water lead to restricting the heat releasing, thus, the H decreased. Wind speed has the most important contribution of H according to the largest correlation coefficient ($=0.98$) between U and H. In another word, wind speed plays a more significant role in the heat transfer compared to K_d on

the Namtso Lake. The result of the physical control of sensible heat flux was consistent with the small lake near the Namtso Lake investigated by Wang et al., 2015 and Wang et al., 2017.

Actually, the Eq.15 simplify the calculation of H that only consider the T_a and T_s and wind speed. But the real situation is much more complicated than the Eq.15 described. H is also related to the atmospheric stability and the energy exchange via atmosphere advection between the lake and land surfaces (Lofgren & Zhu, 2000).

6.4. The limitations

The field measurement was performed on 25th May 2017 while the acquisition date of S2 matchup data was on 15th May 2017. The difference between data from the two days could induce the major uncertainty. In addition, estimation of the uncertainty generated from IOPs inversion scheme play an important role in the assessment of the ocean colour retrieval algorithm (Salama et al., 2011; Lee et al., 2010). In this study, however, IOPs such as absorption coefficient and backscattering coefficient are not measured could result in the errors originated from the inversion scheme in 2SeaColor model cannot observe. Besides, the atmospheric correction should select carefully.

General errors may originate from the highly dynamic water turbulence and subpixel effect, and the human-induced error when performing the in-situ measurements. Besides, satellite data limited by clouds, also the number of in-situ measurements and the meteorological data that used to calculate the H is excepted cover the whole lake.

Therefore, based on the limitation mentioned above, the following recommendations were given (1) field measurements should cover more areas of the lake, (2) the wind speed data and the air temperature are supposed to use the dedicated model to estimate in order to provide the wind speed map and air temperature map of the lake, (3) the studied time series should extend.

7. CONCLUSIONS

In this study, the 2SeaColor model was employed to estimate the diffuse attenuation coefficient for the underwater downward irradiance in combination with S2 data over Namtso Lake in TP. Based on the results and analysis above, the following conclusions were drawn:

1. The 2SeaColor model is capable of providing a relatively accurate estimation of K_d that is ranging from 0 to 2 m^{-1} in Namtso Lake.
2. The northeast and northwest of the nearshore waters of the lake presented a higher K_d value than the offshore of the lake. This spatial distribution of K_d is attributed to the SPM transported by the inflowed river was enriched in the river mouth. Therefore, the K_d mainly controlled by SPM in Namtso Lake. The temporal distribution of K_d explicated a similar pattern because it is cold months during the studies time series which result in the little activity of the optically significant water constituents.
3. It is not conclusive that the K_d and LST are temporally correlated within the eight studied time series. As for the spatial correlation between K_d and LST, however, K_d of most of the lake areas are significantly correlated with LST.
4. The correlation coefficient between K_d and H is -0.85 for one site in the lake for four days' measurements. Therefore, K_d has an enormous potential to predict the LST or H despite the influential mechanism should vastly investigate.

LIST OF REFERENCES

- Austin, R. W., & Petzold, T. J. (1981). The Determination of the Diffuse Attenuation Coefficient of Sea Water Using the Coastal Zone Color Scanner BT - Oceanography from Space. In J. F. R. Gower (Ed.) (pp. 239–256). Boston, MA: Springer US. https://doi.org/10.1007/978-1-4613-3315-9_29
- Berk, A., Anderson, G. P., Acharya, P. K., Bernstein, L. S., Muratov, L., Lee, J., ... Hoke, M. L. (2006). MODTRAN5: 2006 update. In *Proc. SPIE* (Vol. 6233, p. 62331F).
- Brockmann, C., Doerffer, R., Peters, M., Kerstin, S., Embacher, S., & Ruescas, A. (2016). Evolution of the C2RCC neural network for Sentinel 2 and 3 for the retrieval of ocean colour products in normal and extreme optically complex waters. In *Living Planet Symposium* (Vol. 740, p. 54).
- Brutsaert, W. (1982). Energy Fluxes at the Earth's Surface. In *Evaporation into the Atmosphere* (pp. 128–153). Dordrecht: Springer Netherlands. https://doi.org/10.1007/978-94-017-1497-6_6
- Cairo, C. T., Barbosa, C. C. F., de Moraes Novo, E. M. L., & do Carmo Calijuri, M. (2017). Spatial and seasonal variation in diffuse attenuation coefficients of downward irradiance at Ibitinga Reservoir, São Paulo, Brazil. *Hydrobiologia*, 784(1), 265–282. <https://doi.org/10.1007/s10750-016-2883-7>
- Calijuri, M. C., Dos Santos, A. C. A., & Jati, S. (2002). Temporal changes in the phytoplankton community structure in a tropical and eutrophic reservoir (Barra Bonita, S.P.--Brazil). *Journal of Plankton Research*, 24(7), 617–634. <https://doi.org/10.1093/plankt/24.7.617>
- Chang, G. C., & Dickey, T. D. (2004). Coastal ocean optical influences on solar transmission and radiant heating rate. *Journal of Geophysical Research*, 109(C1), C01020. <https://doi.org/10.1029/2003JC001821>
- Chen, J., Zhang, X., Xing, X., Ishizaka, J., & Yu, Z. (2017). A Spectrally Selective Attenuation Mechanism-Based KparAlgorithm for Biomass Heating Effect Simulation in the Open Ocean. *Journal of Geophysical Research: Oceans*, 9370–9386. <https://doi.org/10.1002/2017JC013101>
- Crosman, E. T., & Horel, J. D. (2009). MODIS-derived surface temperature of the Great Salt Lake. *Remote Sensing of Environment*, 113(1), 73–81. <https://doi.org/10.1016/j.rse.2008.08.013>
- D'Odorico, P., Gonsamo, A., Damm, A., & Schaepman, M. E. (2013). Experimental evaluation of sentinel-2 spectral response functions for NDVI time-series continuity. *IEEE Transactions on Geoscience and Remote Sensing*, 51(3), 1336–1348. <https://doi.org/10.1109/TGRS.2012.2235447>
- Dekker, A. G., Vos, R. J., & Peters, S. W. M. (2002). Analytical algorithms for lake water TSM estimation for retrospective analyses of TM and SPOT sensor data. *International Journal of Remote Sensing*, 23(1), 15–35. <https://doi.org/10.1080/01431160010006917>
- Denman, K. L. (1973). A Time-Dependent Model of the Upper Ocean. *Journal of Physical Oceanography*, 3(2), 173–184. [https://doi.org/10.1175/1520-0485\(1973\)003<0173:ATDMOT>2.0.CO;2](https://doi.org/10.1175/1520-0485(1973)003<0173:ATDMOT>2.0.CO;2)
- Doerffer, R., & Schiller, H. (2007). The MERIS Case 2 water algorithm. *International Journal of Remote Sensing*, 28(3–4), 517–535. <https://doi.org/10.1080/01431160600821127>
- Duntley, S. Q. (1942). The Optical Properties of Diffusing Materials. *Journal of the Optical Society of America*, 32(2), 61. <https://doi.org/10.1364/JOSA.32.000061>
- Duntley, S. Q. (1963). Light in the Sea*. *Journal of the Optical Society of America*, 53(2), 214. <https://doi.org/10.1364/JOSA.53.000214>
- Emery, W. J., & Yu, Y. (1997). Satellite sea surface temperature patterns. *International Journal of Remote Sensing*, 18(2), 323–334. <https://doi.org/10.1080/014311697219097>
- Fleming, D. J. (2006). *EFFECT OF RELATIVE SPECTRAL RESPONSE ON MULTI-SPECTRAL MEASUREMENTS AND NDVI FROM DIFFERENT REMOTE SENSING SYSTEMS*. University of Maryland. Retrieved from <https://drum.lib.umd.edu/bitstream/handle/1903/3313/umi-umd-3147.pdf;jsessionid=802C75B9DBFC0BB835BEAD2288E23339?sequence=1>
- Frankignoul, C., Czaja, A., & L'Heveder, B. (1998). Air–Sea Feedback in the North Atlantic and Surface Boundary Conditions for Ocean Models. *Journal of Climate*, 11(9), 2310–2324. [https://doi.org/10.1175/1520-0442\(1998\)011<2310:ASFITN>2.0.CO;2](https://doi.org/10.1175/1520-0442(1998)011<2310:ASFITN>2.0.CO;2)
- Giardino, C., Pepe, M., Brivio, P. A., Ghezzi, P., & Zilioli, E. (2001). Detecting chlorophyll, Secchi disk depth and surface temperature in a sub-alpine lake using Landsat imagery. *Science of The Total Environment*, 268(1–3), 19–29. [https://doi.org/10.1016/S0048-9697\(00\)00692-6](https://doi.org/10.1016/S0048-9697(00)00692-6)
- Glasgow, H. B., Burkholder, J. M., Reed, R. E., Lewitus, A. J., & Kleinman, J. E. (2004). Real-time remote monitoring of water quality: a review of current applications, and advancements in sensor, telemetry, and computing technologies. *Journal of Experimental Marine Biology and Ecology*, 300(1), 409–448.
- Guan, Z. H., Chen, C. Y., Ou, Y. X., Fan, Y. Q., Zhang, Y. S., Chen, Z. M., ... Zhang, M. T. (1984).

Rivers and lakes in Tibet. *Science and Technology Press, Beijing (in Chinese)*.

- Haginoya, S., Fujii, H., Kuwagata, T., Xu, J., Ishigooka, Y., Kang, S., & Zhang, Y. (2009). Air-Lake Interaction Features Found in Heat and Water Exchanges over Nam Co on the Tibetan Plateau. *Sola*, 5(55279), 172–175. <https://doi.org/10.2151/sola.2009-044>
- Hausmann, U., Czaja, A., & Marshall, J. (2016). Estimates of air-sea feedbacks on sea surface temperature anomalies in the Southern Ocean. *Journal of Climate*, 29(2), 439–454. <https://doi.org/10.1175/JCLI-D-15-0015.1>
- Hu, L., Brunzell, N. A., Monaghan, A. J., Barlage, M., & Wilhelm, O. V. (2014). How can we use MODIS land surface temperature to validate long-term urban model simulations? *Journal of Geophysical Research: Atmospheres*, 119(6), 3185–3201. <https://doi.org/10.1002/2013JD021101>
- Hulst, H. C. van de (Hendrik C. (1981). *Light scattering by small particles*. Dover Publications.
- Imberger, J., & Patterson, J. C. (1980). *Dynamic Reservoir Simulation Model-DYRESM: 5. Transport models for inland and coastal waters*. New York: Academic press.
- Ke, C.-Q., Tao, A.-Q., & Jin, X. (2013). Variability in the ice phenology of Nam Co Lake in central Tibet from scanning multichannel microwave radiometer and special sensor microwave/imager: 1978 to 2013. *Journal of Applied Remote Sensing*, 7(1), 73477. <https://doi.org/10.1117/1.JRS.7.073477>
- Kondo, J. (1975). Air-sea bulk transfer coefficients in diabatic conditions. *Boundary-Layer Meteorology*, 9(1), 91–112. <https://doi.org/10.1007/BF00232256>
- Kratzer, S., Brockmann, C., & Moore, G. (2008). Using MERIS full resolution data to monitor coastal waters — A case study from Himmerfjärden, a fjord-like bay in the northwestern Baltic Sea. *Remote Sensing of Environment*, 112(5), 2284–2300. <https://doi.org/10.1016/j.rse.2007.10.006>
- Kropáček, J., Maussion, F., Chen, F., Hoerz, S., & Hochschild, V. (2013). Analysis of ice phenology of lakes on the Tibetan Plateau from MODIS data. *The Cryosphere*, 7(1), 287–301. <https://doi.org/10.5194/tc-7-287-2013>
- Lami, A., Turner, S., Musazzi, S., Gerli, S., Guilizzoni, P., Rose, N. L., ... Yang, R. (2010). Sedimentary evidence for recent increases in production in Tibetan plateau lakes. *Hydrobiologia*, 648(1), 175–187. <https://doi.org/10.1007/s10750-010-0263-2>
- Laws, E. A. (1997). *Mathematical methods for oceanographers: An introduction*. John Wiley & Sons.
- Lee, Z.-P., Darecki, M., Carder, K. L., Davis, C. O., Stramski, D., & Rhea, W. J. (2005). Diffuse attenuation coefficient of downwelling irradiance: An evaluation of remote sensing methods. *Journal of Geophysical Research*, 110(C2), C02017. <https://doi.org/10.1029/2004JC002573>
- Lee, Z., Du, K., & Arnone, R. (2005). A model for the diffuse attenuation coefficient of downwelling irradiance. *Journal of Geophysical Research*, 110(C2), C02016. <https://doi.org/10.1029/2004JC002275>
- Lee, Z., Arnone, R., Hu, C., Werdell, P. J., & Lubac, B. (2010). Uncertainties of optical parameters and their propagations in an analytical ocean color inversion algorithm. *Applied Optics*, 49(3), 369. <https://doi.org/10.1364/AO.49.000369>
- Lee, Z., Carder, K. L., & Arnone, R. A. (2002). Deriving inherent optical properties from water color: a multiband quasi-analytical algorithm for optically deep waters. *Applied Optics*, 41(27), 5755. <https://doi.org/10.1364/AO.41.005755>
- Lee, Z., Darecki, M., Carder, K. L., Davis, C. O., Stramski, D., & Rhea, W. J. (2005). Diffuse attenuation coefficient of downwelling irradiance: An evaluation of remote sensing methods. *Journal of Geophysical Research C: Oceans*, 110(2), 1–9. <https://doi.org/10.1029/2004JC002573>
- Liu, K., Liu, Y., Jiao, N., Zhu, L., Wang, J., Hu, A., & Liu, X. (2016). Vertical variation of bacterial community in Nam Co, a large stratified lake in central Tibetan Plateau. *Antonie van Leeuwenhoek, International Journal of General and Molecular Microbiology*, 109(10), 1323–1335. <https://doi.org/10.1007/s10482-016-0731-4>
- Liu, X., & Chen, B. (2000). Climatic warming in the Tibetan Plateau during recent decades. *International Journal of Climatology*, 20(14), 1729–1742. [https://doi.org/10.1002/1097-0088\(20001130\)20:14<1729::AID-JOC556>3.0.CO;2-Y](https://doi.org/10.1002/1097-0088(20001130)20:14<1729::AID-JOC556>3.0.CO;2-Y)
- Liu, X., Yao, T., Kang, S., Jiao, N., Zeng, Y., & Liu, Y. (2010). Bacterial community of the largest Oligosaline Lake, Namco on the Tibetan plateau. *Geomicrobiology Journal*, 27(8), 669–682. <https://doi.org/10.1080/01490450903528000>
- Lofgren, B. M., & Zhu, Y. (2000). Surface energy fluxes on the Great Lakes based on satellite-observed surface temperatures 1992 to 1995. *Journal of Great Lakes Research*, 26(3), 305–314. [https://doi.org/10.1016/S0380-1330\(00\)70694-0](https://doi.org/10.1016/S0380-1330(00)70694-0)
- Loiselle, S. A., Bracchini, L., Cózar, A., Dattilo, A. M., Tognazzi, A., & Rossi, C. (2009). Variability in photobleaching yields and their related impacts on optical conditions in subtropical lakes. *Journal of*

- Photochemistry and Photobiology B: Biology*, 95(2), 129–137.
<https://doi.org/10.1016/j.jphotobiol.2009.02.002>
- Ma, Y., Zhu, Z., Zhong, L., Wang, B., Han, C., Wang, Z., ... Hu, Z. (2014). Combining MODIS, AVHRR and in situ data for evapotranspiration estimation over heterogeneous landscape of the Tibetan Plateau. *Atmospheric Chemistry and Physics*, 14(3), 1507–1515. <https://doi.org/10.5194/acp-14-1507-2014>
- Majozi, N. P., Suhyb, M., Bernard, S., Harper, D. M., & Ghirmai, M. (2014). Remote Sensing of Environment Remote sensing of euphotic depth in shallow tropical inland waters of Lake Naivasha using MERIS data. *Remote Sensing of Environment*, 148, 178–189.
<https://doi.org/10.1016/j.rse.2014.03.025>
- Mobley, C. D. (1994). Light and water: radiative transfer in natural waters. Academic press.
- Morel, A., & Antoine, D. (1994). Heating Rate within the Upper Ocean in Relation to its Bio-optical State. *Journal of Physical Oceanography*, 24(7), 1652–1665. [https://doi.org/10.1175/1520-0485\(1994\)024<1652:HRWTUO>2.0.CO;2](https://doi.org/10.1175/1520-0485(1994)024<1652:HRWTUO>2.0.CO;2)
- Nima, C., Hamre, B., Frette, Ø., Erga, S. R., Chen, Y.-C., Zhao, L., ... Stamnes, J. J. (2016). Impact of particulate and dissolved material on light absorption properties in a High-Altitude Lake in Tibet, China. *Hydrobiologia*, 768(1), 63–79. <https://doi.org/10.1007/s10750-015-2528-2>
- O'Reilly, J. E., Maritorena, S., Mitchell, B. G., Siegel, D. A., Carder, K. L., Garver, S. A., ... McClain, C. (1998). Ocean color chlorophyll algorithms for SeaWiFS. *Journal of Geophysical Research: Oceans*, 103(C11), 24937–24953. <https://doi.org/10.1029/98JC02160>
- Pu, H., Liu, D., Qu, J.-H., & Sun, D.-W. (2017). Applications of Imaging Spectrometry in Inland Water Quality Monitoring—a Review of Recent Developments. *Water, Air, & Soil Pollution*, 228(4), 131. <https://doi.org/10.1007/s11270-017-3294-8>
- Read, J. S., Hamilton, D. P., Desai, A. R., Rose, K. C., MacIntyre, S., Lenters, J. D., ... Wu, C. H. (2012). Lake-size dependency of wind shear and convection as controls on gas exchange. *Geophysical Research Letters*, 39(9), n/a-n/a. <https://doi.org/10.1029/2012GL051886>
- Read, J. S., Rose, K. C., Winslow, L. A., & Read, E. K. (2015). A method for estimating the diffuse attenuation coefficient (KdPAR) from paired temperature sensors. *Limnology and Oceanography: Methods*, 13(2), 53–61. <https://doi.org/10.1002/lom3.10006>
- Ruddick, K. G., De Cauwer, V., Park, Y.-J., & Moore, G. (2006). Seaborne measurements of near infrared water-leaving reflectance: The similarity spectrum for turbid waters. *Limnol. Oceanogr*, 51(2), 1167–1179. Retrieved from <http://ir.polytechnic.edu.na/bitstream/handle/10628/216/ve.pdf?sequence=1&isAllowed=y>
- Salama, M. S., Dekker, A., Su, Z., Mannaerts, C. M., & Verhoef, W. (2009). Deriving inherent optical properties and associated inversion-uncertainties in the Dutch Lakes. *Hydrology and Earth System Sciences*, 13(7), 1113–1121. <https://doi.org/10.5194/hess-13-1113-2009>
- Salama, M. S., Mélin, F., & Van der Velde, R. (2011). Ensemble uncertainty of inherent optical properties. *Optics Express*, 19(18), 16772. <https://doi.org/10.1364/OE.19.016772>
- Salama, M. S., & Shen, F. (2010). Simultaneous atmospheric correction and quantification of suspended particulate matters from orbital and geostationary earth observation sensors. *Estuarine, Coastal and Shelf Science*, 86(3), 499–511. <https://doi.org/10.1016/J.ECSS.2009.10.001>
- Salama, M. S., & Stein, A. (2009). Error decomposition and estimation of inherent optical properties. *Applied Optics*, 48(26), 4947. <https://doi.org/10.1364/AO.48.004947>
- Salama, M. S., & Verhoef, W. (2015). Two-stream remote sensing model for water quality mapping: 2SeaColor. *Remote Sensing of Environment*, 157, 111–122. <https://doi.org/10.1016/j.rse.2014.07.022>
- Simon, A., & Shanmugam, P. (2016). Estimation of the spectral diffuse attenuation coefficient of downwelling irradiance in inland and coastal waters from hyperspectral remote sensing data: Validation with experimental data. *International Journal of Applied Earth Observation and Geoinformation*, 49, 117–125. <https://doi.org/10.1016/j.jag.2016.02.003>
- Sterckx, S., Knaeps, E., Adriaensen, S., Reusen, I., Keukelaere, L. De, & Hunter, P. (2015). Opera : an Atmospheric Correction for Land and Water. *Proceedings of the Sentinel-3 for Science Workshop*, (1), 3–6. Retrieved from http://odnature.naturalsciences.be/downloads/publications/Sterckxetal_2015S3Forscience_finalv2-1.pdf
- Sterckx, S., Knaeps, E., Kratzer, S., & Ruddick, K. (2014). SIMilarity Environment Correction (SIMEC) applied to MERIS data over inland and coastal waters. *Remote Sensing of Environment* (Vol. 157). <https://doi.org/10.1016/j.rse.2014.06.017>

- Stramska, M., & Zuzewicz, A. (2013). Influence of the parametrization of water optical properties on the modelled sea surface temperature in the Baltic Sea**This work was supported by the SatBaltyk project funded by the European Union through the European Regional Development Fund (contract No. POIG.01.01.02-22-011/09 entitled “The Satellite Monitoring of the Baltic Sea Environment”). *Oceanologia*, 55(1), 53–76. <https://doi.org/10.5697/oc.55-1.053>
- Su, Z., Levizzani, V., Rott, H., Wagner, W., Salama, M., Parodi, G., & Wang, L. (2011). *Treatise on Water Science*. (Peter Wilderer, Ed.). Oxford Academic Press. Retrieved from [https://blackboard.utwente.nl/bbcswebdav/pid-1013114-dt-content-rid-2369044_2/courses/M17-WREM-102/Documents/Remote sensing of water quality References Su etal 2011/42_TOWS_EOWC_Elsevier2011.pdf](https://blackboard.utwente.nl/bbcswebdav/pid-1013114-dt-content-rid-2369044_2/courses/M17-WREM-102/Documents/Remote%20sensing%20of%20water%20quality%20References%20Su%20etal%202011/42_TOWS_EOWC_Elsevier2011.pdf)
- Teillet, P. M., Fedosejevs, G., Thome, K. J., & Barker, J. L. (2007). Impacts of spectral band difference effects on radiometric cross-calibration between satellite sensors in the solar-reflective spectral domain. *Remote Sensing of Environment*, 110(3), 393–409. <https://doi.org/10.1016/j.rse.2007.03.003>
- Tiwari, S. P., & Shanmugam, P. (2014). A Robust Algorithm to Determine Diffuse Attenuation Coefficient of Downwelling Irradiance From Satellite Data in Coastal Oceanic Waters. *IEEE Journal of Selected Topics in Applied Earth Observations and Remote Sensing*, 7(5), 1616–1622. <https://doi.org/10.1109/JSTARS.2013.2282938>
- Vanhellemont, Q., & Ruddick, K. (2016). ACOLITE FOR SENTINEL-2: AQUATIC APPLICATIONS OF MSI IMAGERY. *ESA Special Publication*, 9–13. Retrieved from https://odnature.naturalsciences.be/downloads/publications/vanhellemontruddick_esa_lps2016_coastalapplications_final_header.pdf
- Vermote, E., Tanré, D., Deuzé, J. L., Herman, M., Morcrette, J. J., & Kotchenova, S. Y. (2006). Second Simulation of a Satellite Signal in the Solar Spectrum -Vector (6SV). Retrieved from http://6s.ltdri.org/files/tutorial/6S_Manual_Part_1.pdf
- Vollenweider, R. A. (1982). *Eutrophication of waters : monitoring, assessment and control*. (O. for E. C. and Development, Ed.). Paris : [Washington, D.C: Organisation for Economic Co-operation and Development ; Sold by OECD Publications and Information Center].
- Vorosmarty, C. J., McIntyre, P. B., Gessner, M. O., Dudgeon, D., Prusevich, A., Green, P., ... Davies, P. M. (2010). Global threats to human water security and river biodiversity. *Nature*, 467(7315), 555–561. Retrieved from <http://dx.doi.org/10.1038/nature09440>
- Wang, B., Ma, Y., Chen, X., Ma, W., Su, Z., & Menenti, M. (2015). Observation and simulation of lake-air heat and water transfer processes in a high-altitude shallow lake on the Tibetan Plateau. *Journal of Geophysical Research: Atmospheres*, 120(24), 12327–12344. <https://doi.org/10.1002/2015JD023863>
- Wang, B., Ma, Y., Ma, W., & Su, Z. (2017). Physical controls on half-hourly, daily, and monthly turbulent flux and energy budget over a high-altitude small lake on the Tibetan Plateau. *Journal of Geophysical Research*, 122(4), 2289–2303. <https://doi.org/10.1002/2016JD026109>
- Wang, J., Zhu, L., Daut, G., Ju, J., Lin, X., Wang, Y., & Zhen, X. (2009). Investigation of bathymetry and water quality of Lake Nam Co, the largest lake on the central Tibetan Plateau, China. *Limnology*, 10(2), 149–158. <https://doi.org/10.1007/s10201-009-0266-8>
- Wang, J., Zhu, L., Wang, Y., Ju, J., Xie, M., & Daut, G. (2010). Comparisons between the chemical compositions of lake water, inflowing river water, and lake sediment in Nam Co, central Tibetan Plateau, China and their controlling mechanisms. *Journal of Great Lakes Research*, 36(4), 587–595. <https://doi.org/10.1016/j.jglr.2010.06.013>
- Wang, M., Son, S. H., & Shi, W. (2009). Evaluation of MODIS SWIR and NIR-SWIR atmospheric correction algorithms using SeaBASS data. *Remote Sensing of Environment*, 113(3), 635–644. <https://doi.org/10.1016/j.rse.2008.11.005>
- Wu, Y., Platt, T., Tang, C., & Sathyendranath, S. (2008). Regional differences in the timing of the spring bloom in the Labrador Sea. *Marine Ecology Progress Series*, 355, 9–20. <https://doi.org/10.3354/meps07233>
- Wu, Y., Tang, C. C. L., Sathyendranath, S., & Platt, T. (2007). The impact of bio-optical heating on the properties of the upper ocean: A sensitivity study using a 3-D circulation model for the Labrador Sea. *Deep Sea Research Part II: Topical Studies in Oceanography*, 54(23–26), 2630–2642. <https://doi.org/10.1016/j.dsr2.2007.08.019>
- Xiao, F., Ling, F., Du, Y., Feng, Q., Yan, Y., & Chen, H. (2013). Evaluation of spatial-temporal dynamics in surface water temperature of Qinghai Lake from 2001 to 2010 by using MODIS data. *Journal of Arid Land*, 5(4), 452–464. <https://doi.org/10.1007/s40333-013-0188-5>
- Yong, W., Liping, Z., Junbo, W., Jianting, J., & Xiao, L. (2012). The spatial distribution and sedimentary

- processes of organic matter in surface sediments of Nam Co, Central Tibetan Plateau. *Geography December*, 5736, 4753–4764. <https://doi.org/10.1007/s11434-012-5500-9>
- Yu, X., Salama, M. S., Shen, F., & Verhoef, W. (2016). Retrieval of the diffuse attenuation coefficient from GOCI images using the 2SeaColor model: A case study in the Yangtze Estuary. *Remote Sensing of Environment*, 175, 109–119. <https://doi.org/10.1016/j.rse.2015.12.053>
- Zhang, R. H., Gao, C., Kang, X., Zhi, H., Wang, Z., & Feng, L. (2015). ENSO Modulations due to Interannual Variability of Freshwater Forcing and Ocean Biology-induced Heating in the Tropical Pacific. *Scientific Reports*, 5(November), 1–11. <https://doi.org/10.1038/srep18506>
- Zhang, T., & Fell, F. (2007). An empirical algorithm for determining the diffuse attenuation coefficient K_d in clear and turbid waters from spectral remote sensing reflectance. *Limnology and Oceanography: Methods*, 5(12), 457–462. <https://doi.org/10.4319/lom.2007.5.457>
- Zheng, Z., Ren, J., Li, Y., Huang, C., Liu, G., Du, C., & Lyu, H. (2016). Remote sensing of diffuse attenuation coefficient patterns from Landsat 8 OLI imagery of turbid inland waters: A case study of Dongting Lake. *Science of the Total Environment*, 573, 39–54. <https://doi.org/10.1016/j.scitotenv.2016.08.019>
- Zhengming Wan, & Dozier, J. (1996). A generalized split-window algorithm for retrieving land-surface temperature from space. *IEEE Transactions on Geoscience and Remote Sensing*, 34(4), 892–905. <https://doi.org/10.1109/36.508406>
- Zhu, D. ., Meng, X. ., Zhao, X. ., Shao, Z. ., Feng, X. ., Yang, C. ., ... Zhang, W. . (2004). *On the Quaternary Environmental Evolution of Nam Co Area, Tibet*. Beijing: Geology Press.